
Properties of Galaxies around AGNs with Most Massive Supermassive Black Hole Revealed by the Clustering Analysis

Yuji Shirasaki^{1,2}, Yutaka Komiya³, Masatoshi Ohishi^{1,2} and Yoshihiko Mizumoto^{1,2}

¹National Astronomical Observatory of Japan, 2-21-1 Osawa, Mitaka, Tokyo 181-8588, Japan

²Department of Astronomical Science, School of Physical Sciences, SOKENDAI (The Graduate University for Advanced Studies), Okazaki 444-8787, Japan

³Research center for the early universe, University of Tokyo, 7-3-1 Hongo, Bunkyo-ku Tokyo, 113-0033, Japan

*E-mail: yuji.shirasaki@nao.ac.jp

Received (reception date); Accepted (acceptation date)

Abstract

We present results of the clustering analysis between active galactic nuclei (AGNs) and galaxies at redshift 0.1–1.0, which was performed for investigating properties of galaxies associated with the AGNs and revealing the nature of fueling mechanism of supermassive black holes (SMBHs). We used 8059 SDSS AGNs/QSOs for which virial masses of individual SMBHs were measured, and divided them into four mass groups. Cross-correlation analysis was performed to reconfirm our previous result that cross-correlation length increases with SMBH mass M_{BH} ; we obtained consistent results. A linear bias of AGN for each mass group was measured as 1.47 for $M_{\text{BH}} = 10^{7.5} - 10^{8.2} M_{\odot}$ and 3.08 for $M_{\text{BH}} = 10^9 - 10^{10} M_{\odot}$. The averaged color and luminosity distributions of galaxies around the AGNs/QSOs were also derived for each mass group. The galaxy color $D_{\text{opt-IR}}$ was estimated from an SED constructed with a merged SDSS and UKIDSS catalog. The distributions of color and luminosity were derived by a subtraction method, which does not require redshift information of galaxies. The main results of this work are: (1) a linear bias increases by a factor two from the lower mass group to the highest mass group; (2) the environment around AGNs with the most massive SMBH ($M_{\text{BH}} > 10^9 M_{\odot}$) is dominated by red sequence galaxies; (3) marginal indication of decline in luminosity function at dimmer side of $M_{\text{IR}} > -19.5$ is found for galaxies around AGNs with $M_{\text{BH}} = 10^{8.2} - 10^9 M_{\odot}$ and nearest redshift group ($z = 0.1 - 0.3$). These results indicate that AGNs with the most massive SMBHs reside in haloes where large fraction of galaxies have been transited to the red sequence. The accretion of hot halo gas as well as recycled gas from evolving stars can be one of the plausible mechanisms to fuel the SMBHs above $\sim 10^9 M_{\odot}$.

Key words: astronomical databases: miscellaneous — galaxies: active — large-scale structure of universe — quasars: general — virtual observatory tools

1 Introduction

There are a lot of observational evidences that a Supermassive Black Hole (hereafter SMBH) is located in the center of all but

the smallest galaxies (Richstone et al. 1998). Although the evolution mechanism of SMBH is still not well known, a recent growing evidence suggests that there is a strong link between

the growth of SMBH and the star formation in the host galaxy. One of the observational evidence is the similarity between the evolutions of black hole accretion rate and the star formation rate of galaxies (e.g., Madau et al. 1996; Boyle et al. 1998; Ueda et al. 2003; Zheng et al. 2009). Another important evidence is the correlation between mass of the SMBH (M_{BH}) and mass (M_b) / velocity dispersion (σ) of the bulge component of its host galaxy (Magorrian et al. 1998; Ferrarese & Merritt 2000; Gebhardt et al. 2000; Ho 2007). These relations indicate that BHs and bulges coevolve regulating each others growth (see the recent review by Kormendy & Ho 2013, and references therein).

According to the theoretical works (e.g., King 2014), mass of a SMBH can be regulated by its own outflow from an active galactic nucleus (AGN) in a way that the interstellar gas is expelled far away from the host galaxy once M_{BH} reaches to the critical mass given by the $M_{\text{BH}}-\sigma$ relation. As a result both the star formation in the bulge and mass accretion onto the SMBH are terminated. Therefore understanding the evolution mechanism of SMBHs and AGN phenomenon is crucial to shed light on the evolution of galaxies.

The most important open questions are the nature of the fueling of SMBHs and triggering mechanisms of AGNs. The following three modes have been proposed for transferring gas onto the center of galaxy (e.g., Croton et al. 2006; Lagos et al. 2008; Keres et al. 2009; Fanidakis et al. 2013):

First one is a secular mode which arise through internal dynamical processes in the disk such as a bar instability or external processes of galaxy interactions. Some authors claim that low luminosity AGNs hosted by late type disk galaxies are driven by this mode (see review by Kormendy & Kennicutt 2004, and references therein).

Second one is a merger mode in which gravitational torques induced by galaxy-galaxy major/minor mergers drive inflows of cold gas toward the center of galaxies, triggering the central starbursts and also accretion on to the SMBH, i.e. AGN (e.g., Hopkins et al. 2008). There are observational evidence that some of the luminous AGN, i.e. QSOs, are likely triggered by a major merger (e.g., Sanders et al. 1988; Treister et al. 2012).

There has been an observational evidence that AGN activity is enhanced for close companion galaxies which are assumed to be undergoing early stage of interaction (Silverman et al. 2011). However, the fraction of such close pairs is only $\sim 18\%$, and visual inspection of HST image revealed that $\sim 85\%$ of AGN host galaxies show no strong distortions on their morphologies (Cisternas et al. 2011). Thus galaxy interaction including major merger cannot be the only mechanism for fueling SMBHs, at least for AGNs with moderate luminosity sampled by Silverman et al. (2011) and Cisternas et al. (2011). Kaviraj (2014) analyzed SDSS data to probe the role of minor mergers in driving stellar mass and BH growth in galaxies, and suggest

that around half of the star formation activity is triggered by the minor-merger process.

Third one is a hot halo mode which is characterized by quiescent accretion of gas from the hot halo (Keres et al. 2009; Fanidakis et al. 2013). In this mode the accretion rate is lower than the other two modes. However it becomes increasingly effective accretion mode at higher dark matter halo masses of $M_h > 10^{12.5} M_\odot$, as the accretion by the other two modes becomes inefficient due to AGN feedback. Thus larger fraction of SMBHs are expected to evolve through the hot halo mode as the host halo mass increases above $M_h > 10^{12.5} M_\odot$, and the corresponding mass of SMBH is $> 10^9 M_\odot$ (Fanidakis et al. 2013b).

Due to the lower accretion rate, the expected AGN luminosity in this mode is typically lower than those of the other two modes in a dark matter halo with the same mass. Observationally such accretion is often associated with BHs that are characterized by very low radiative efficiency.

Kauffmann et al. (2009) observationally found that there are two distinct modes in BH growth. One is associated with galaxy bulges that are undergoing significant star formation, and the other is associated with those with little or no on-going star formation. The former one could be related with the star formation induced by secular and/or merger mode, and the latter with the hot halo mode.

In addition to the three modes, a model of accretion of recycled gas from evolving star has been studied (Ciotti & Ostriker 2001, 2007). According to this model, the recycled gas accumulates within a galaxy under the influence of gas heating from Type Ia supernovae, and a fraction of the gas intermittently accretes to the central SMBH under the effect of AGN feedback. With this scenario the central SMBH grows up to $10^{9.5} M_\odot$ in giant ellipticals.

The mass of dark matter halo in which SMBH resides can be estimated through the large-scale environments. As an estimator of large-scale environments, cross-correlation length and/or a bias parameter are usually used. The absolute bias of AGNs distribution relative to that of the dark matter can be derived from the observed two point correlation function, which is then used to estimate mass of the dark matter halo.

Ross et al. (2009) performed correlation analysis for SDSS QSOs with redshift from 0.3 to 2.2, and obtained a result that the QSOs inhabit dark matter haloes of constant mass of $\sim 2 \times 10^{12} h^{-1} M_\odot$ at any redshifts. Combining this observational result with the theoretical work by Fanidakis et al. (2013), the optical AGNs/QSOs are expected to be mostly powered by either secular or merger mode. It is also inferred that they appear only in the dark matter halo of which the mass does not exceed a critical mass that is determined by the AGN feedback.

Hickox et al. (2009) analyzed the data of radio, X-ray, and IR detected AGN samples, and found that the correspond-

ing masses of dark matter haloes are $\sim 10^{13.5} h^{-1} M_{\odot}$, $\sim 10^{13.0} h^{-1} M_{\odot}$, and $\sim 10^{12.0} h^{-1} M_{\odot}$, respectively. Krumpe et al. (2012) also derived the halo mass for the X-ray selected ROSAT AGNs and the optically selected SDSS AGNs, and they obtained $\sim 10^{13.2} h^{-1} M_{\odot}$ and $\sim 10^{12.7} h^{-1} M_{\odot}$, respectively.

Shen et al. (2011) studied the dependence of quasar clustering on luminosity, mass of SMBH, quasar color, and radio loudness. They did not find significant dependence on either luminosity, mass, or color, while they marginally found that the most luminous and most massive QSOs are more strongly clustered than the remainder of the sample at ~ 2 sigma level, and radio-loud QSOs are more strongly clustered than radio-quiet QSOs.

Many other studies on clustering and/or environment of AGNs/QSOs have been reported elsewhere (e.g., Croom et al. 2005; Coil et al. 2009; Silverman et al. 2009; Donoso et al. 2010; Allevalo et al. 2011; Bradshaw et al. 2011; Mountrichas et al. 2013; Zhang et al. 2013; Georgakakis et al. 2014).

All these studies indicates that some types of AGNs such as those bright in the radio and/or X-ray band inhabits relatively larger dark matter haloes than optically bright AGNs, and at least part of them may be fueled by a different mechanism such as hot halo mode or accretion of recycled gas from evolved stars.

To investigate the relation between the environment and intrinsic properties of AGNs with better accuracy, we have developed a clustering analysis method which does not require measurements of galaxy redshift and thus can utilize all the galaxies detected in the imaging data (Shirasaki et al. 2011; Komiya et al. 2013). Komiya et al. (2013) examined dependence of AGN-galaxy clustering on BH mass, and found an indication of an increasing trend of cross-correlation length above $10^{8.2} M_{\odot}$.

In this paper, following the result of Komiya et al. (2013), we study the properties of galaxies, such as color and luminosity function, around AGNs and its dependence on BH mass by combining optical and near infrared dataset of SDSS and UKIDSS survey. We also derived AGN bias parameter to be compared with other studies.

It is expected that, if the increase of clustering strength for AGNs with higher BH mass is due to the prominence of hot halo mode, most of the galaxies around the AGNs are in red sequence since they reside in haloes where gas cooling and star formation have been shut off by AGN feedback. Accretion of recycled gas from evolving stars may overcome in such a circumstance. Which accretion occurs may depends on the availability of the gas accumulated inside the galaxy and the strength of the AGN feedback. As another possibility, if the AGNs with the most massive SMBH are mostly fueled by mergers with gas-rich galaxies, the environment of the AGNs may be dominated with gas-rich blue star-forming galaxies.

Although it is already known that the massive dark matter

halos are dominated by massive red galaxies (e.g Zehavi et al. 2011) and it may be inferred that those red galaxies are the cause of increase in clustering found by Komiya et al. (2013), such speculation has not been proven by any observations so far. This work gives the first observational evidence about the nature of galaxies around the AGNs as a function of BH mass based on statistically significant number of samples, and provides an important clue to identify the feeding mechanism of the most massive SMBH.

Throughout this paper, we assume a cosmology with $\Omega_m = 0.3$, $\Omega_{\lambda} = 0.7$, $h = 0.7$ and $\sigma_8 = 0.8$. All magnitudes are given in the AB system. All the distances are measured in comoving coordinates. The correlation length is presented in unit of h^{-1} Mpc.

2 Datasets

2.1 AGNs

The AGN samples were extracted from two AGN properties catalogs created by Shen et al. (2011) and Greene et al. (2007a). These catalog contains virial mass estimates of SMBHs, which were measured from the FWHM of emission lines and continuum flux density. We examined systematic difference of the mass estimates between the two catalogs by extracting AGNs which are contained in both of the catalogs. As shown in Figure 1, the mass estimates of Greene et al. (2007a) M_{G07} is relatively lower than the estimates of Shen et al. (2011) M_{S11} by 0.5 dex. We therefore calibrated M_{G07} with M_{S11} using the following formula:

$$M'_{G07} = (M_{G07} - 1.06)/0.806. \quad (1)$$

We used M'_{G07} as mass estimates of AGNs which are included only in the catalog of Greene et al. (2007a). For the other AGNs, we used M_{S11} as their mass estimates.

In this work the range of redshift is restricted to 0.1–1.0, and mass of SMBH is restricted to the range of $10^{6.5} - 10^{10} M_{\odot}$. The redshift and mass distributions of AGNs used in this work are shown in Figures 2–4. The AGN samples from Greene et al. (2007a) mostly comprise lower redshift and lower mass samples. All the samples are divided into 12 groups shown in Figure 2, and analysis are performed for each group with enough statistics or a combined group. Sample selection is applied following the criteria described in section 2.3. The number of analyzed AGNs is 991 from Greene et al. (2007a), 7068 from Shen et al. (2011), and 8059 in total.

2.2 Galaxies

The galaxy samples were retrieved from Virtual Observatory (VO) services of SDSS DR8 (Aihara et al. 2011) and UKIDSS DR9 LAS catalog. The UKIDSS project is defined in Lawrence

et al. (2007). The data retrieval and creation of the merged catalog were performed for each AGN. The JVO command line tool (jc client¹) was used to automate the data retrieval. The following criteria are used to retrieve the galaxy sample: For SDSS catalog data of which `resolveStatus` attribute equals to 257 or 258, which corresponds to select unique objects, are retrieved. For UKIDSS LAS catalog data of which `mergedClass` attribute equals to 1 or -3, which corresponds to select objects flagged as “Galaxy” or “Probable galaxy”, are retrieved. For both catalog data within 1 degree from the AGN coordinates are retrieved.

Photometric magnitude used in this work is an aperture magnitude in 2 arcsec diameter for both SDSS and UKIDSS. Due to the difference of the point spread functions (PSF) between the two surveys (~ 1.3 arcsec for SDSS in FWHM of PSF, ~ 0.8 arcsec for UKIDSS), color measurements suffer a systematic error especially for objects whose apparent size exceeds the aperture size. In this work the comparisons of galaxy color are made for two samples of lower and higher BH mass, and both of the samples are equally affected by the error of the color estimates. Thus the inaccuracy in the color estimates is not so harmless to derive the relative difference of the distributions of galaxy color.

The two catalogs were merged into a single one. In creating the merged catalog, UKIDSS objects detected in the K band data were used as a reference, and a nearest neighbor was selected from the SDSS catalog within 2 arcsec distance for each UKIDSS object. The UKIDSS objects for which SDSS counterpart was not found were preserved in the merged catalog, while the SDSS objects which were not selected as a counterpart were not included in the merged catalog. Thus our galaxy samples are K-band selected ones.

2.3 Data selection

Data selection was applied to the AGN datasets to ensure their quality as follows: at first, coverage of the SDSS and UKIDSS galaxy samples were investigated by using the window function for SDSS and frame metadata describing the region of observation for UKIDSS. Regions outside the observed area were identified as a dead region.

We found that some of the UKIDSS galaxy samples were spurious events caused by cosmic rays, bright stars, or unknown reason. The area that contains the spurious events was identified by looking for a high density region in the count map of the samples detected in the K-band and not detected in SDSS. Those areas were taken as dead regions as well.

The fractions of the dead region were calculated as a function of projected distance from the AGN position with 0.2 Mpc bin width. If the fraction exceeds 0.2 at a projected distance less than 5 Mpc, the AGN dataset was removed from the samples.

Otherwise the fractions are used to correct the effective area in deriving the number density of galaxies.

Next we examined the uniformity of the galaxy number density around AGN. Since the number of galaxies associated with the AGNs is usually much smaller than the total number of background/foreground galaxies, a flat distribution is expected for the number density as a function of distance from AGN. If there exist a cluster/group of galaxies or stars in front of the AGN field, it can produce strong fluctuation in the distribution of number density. Inhomogeneity of the depth of observations can also produce discontinuous density distribution.

To reduce a false signal produced by those cases, we calculated three parameters, χ^2 , σ_{\max} , and B_{QG} , and they were used to filter the datasets showing non-uniformity in number density. The parameter χ^2 is a square sum of the deviation from a flat distribution, and the parameter σ_{\max} is a maximum deviation from the average density calculated at a distance range from 2 to 5 Mpc. The adapted criteria are $\chi^2/(n-1) \leq 3.0$ and $\sigma_{\max} \leq 5$, where n is the number of data points in the galaxy number density distribution. B_{QG} was calculated as (Longair & Seldner 1979),

$$B_{\text{QG}} = \frac{3 - \gamma}{2\pi} \frac{N_{\text{total}} - N_{\text{bg}}}{\rho_0}, \quad (2)$$

where N_{total} is the total number of galaxies at projected distance less than 1 Mpc from AGN, N_{bg} is the expected number of background/foreground galaxies which are not associated with the AGN and is estimated from the number density at $r_p = 3.0$ – 5.0 Mpc, ρ_0 is the average number density of observed galaxy at the AGN redshift. This parameter is usually used to estimate the clustering strength, but here it is used to remove datasets showing extraordinary large positive/negative excess density around AGNs. The criterion adapted is $-10000 \leq B_{\text{QG}} \leq 10000$. Only two samples were discarded with this selection. We checked that the samples for which clustering strength is smaller than ~ 80 Mpc in term of correlation length don't give rise a prominent fluctuation detected with the above criteria in the galaxy density histogram. As such, these criteria are almost free from selection bias caused by the clustering strength itself at the source.

To maximize the signal-to-noise ratio, we removed datasets of shallow observations based on the parameter ρ_0 , which is an average number density of galaxies at the AGN redshift; ρ_0 is calculated from the luminosity function which is parametrized as a function of redshift z and rest-frame wavelength λ as discussed in Komiya et al. (2013). We adapted a criteria of $\rho_0 \geq 10^{-4} \text{ Mpc}^{-3}$.

The total number of AGN datasets that have passed above criteria is 8059 out of the original number of 9986. About 20% of datasets are discarded. Among the 8059 samples, $\sim 80\%$ of the samples overlap with the Komiya et al. (2013) samples.

¹ http://jvo.nao.ac.jp/jc_client/

3 Analysis Method

3.1 Correlation length

The analysis method used for calculating the AGN-galaxy cross-correlation function is completely the same as that used in Komiya et al. (2013), which is briefly described here.

The cross-correlation function of AGNs and galaxies $\xi(r)$ can be expressed as an excess in number density of galaxies $\rho(r)$ relative to the average density ρ_0 at the AGN redshift,

$$\xi(r) = \frac{\rho(r)}{\rho_0} - 1, \quad (3)$$

where r represents the distance from an AGN. We assume the power-law form for the cross-correlation function,

$$\xi(r) = \left(\frac{r}{r_0}\right)^{-\gamma}, \quad (4)$$

where r_0 is the correlation length and γ is the power-law index fixed to 1.8, which is a canonical value measured by many other clustering study of galaxies and QSOs. The projected cross-correlation function $\omega(r_p)$ is calculated by integrating Equation (3) as

$$\begin{aligned} \omega(r_p) &= 2 \int_0^\infty \xi(r_p, \pi) d\pi = 2 \int_{r_p}^\infty \frac{r\xi(r)}{\sqrt{r^2 - r_p^2}} dr \\ &= r_p \left(\frac{r_0}{r_p}\right)^\gamma \frac{\Gamma(\frac{1}{2})\Gamma(\frac{\gamma-1}{2})}{\Gamma(\frac{\gamma}{2})}, \end{aligned} \quad (5)$$

where π and r_p are distance along and perpendicular to the line of sight, respectively, and Γ is the gamma function. $\omega(r_p)$ can be derived observationally from the surface density of galaxies $n(r_p)$ as

$$\omega(r_p) = \frac{n(r_p) - n_{bg}}{\rho_0}, \quad (6)$$

where n_{bg} represents the surface density of background/foreground galaxies which are unassociated with the corresponding AGN. From Equations (5) and (6), the surface density of galaxies around an AGN can be modeled as

$$n(r_p) = C(\gamma) \cdot \rho_0 \cdot r_p \left(\frac{r_0}{r_p}\right)^\gamma + n_{bg}, \quad (7)$$

where the term of the gamma function is represented by $C(\gamma)$. Fitting this model function to the observed surface density, we can obtain the best estimates of r_0 and n_{bg} . As already mentioned, γ is fixed to 1.8 and ρ_0 is calculated from the empirical formula of galaxy luminosity function. The details of the parametrized luminosity function are described in Komiya et al. (2013). Since the clustering signal is too weak to obtain meaningful parameter values for each AGN dataset, we applied the fitting to the average of $n(r_p)$ and ρ_0 for a given AGN group.

The uncertainty of r_0 is calculated as a root sum square of one sigma statistical error and systematic error derived from the uncertainty of ρ_0 as discussed in Komiya et al. (2013). The uncertainty related with an intrinsic variance of clustering is also estimated from a difference between the cross correlation

lengths calculated for two independent sub samples which are constructed by dividing the original samples.

It should be noted that the cross-correlation length obtained by this method is not a simple average for the AGN group, but an average weighted with ρ_0 . Thus the result is biased to the low- z AGN samples.

3.2 AGN absolute bias

The linear bias of AGNs relative to the dark matter distribution can be derived from the cross-correlation length between AGNs and galaxies as follows: Assuming linear bias, the autocorrelation function of AGNs ξ_{AA} is related with the cross-correlation function between AGNs and galaxies ξ_{AG} in the form,

$$\xi_{AA} = \xi_{AG}^2 / \xi_{GG}, \quad (8)$$

where ξ_{GG} is the autocorrelation function of galaxies. The autocorrelation function of galaxies depends on galaxies color and luminosity, and measured by Zehavi et al. (2011) as $\xi_{GG,blue} = (r/3.6 h^{-1} \text{Mpc})^{-1.7}$ and $\xi_{GG,red} = (r/6.6 h^{-1} \text{Mpc})^{-1.9}$ for blue and red galaxies with brightness of $-20 < M_r < -19$. The luminosity dependence is small in the range of $-22 < M_r < -17$, while for galaxies with $M_r < -22$ the autocorrelation function significantly changes to the form of $\xi_{GG,red} = (r/10.7 h^{-1} \text{Mpc})^{-1.9}$. In order to take into account the difference of blue/red/brightest galaxy fraction in the samples we calculated the autocorrelation function of galaxies with the following formulas:

$$\xi_{GG} = f_{red}\xi_{GG,red} + f_{blue}\xi_{GG,blue} + f_{bright}\xi_{GG,bright}, \quad (9)$$

where f_{red} , f_{blue} , f_{bright} is a fraction of red, blue, and brightest galaxies in the sample which are measured as described in the next section. The autocorrelation function of AGN is calculated by using Equation (8) and (9), and fitted to a power law function of the form of $\xi_{AA} = (r/r_{AA})^{-\gamma}$.

The linear bias of AGNs b is calculated as (Koutoulidis et al. 2013):

$$b = \frac{\sigma_{8,AGN}}{\sigma_{8,DM}}, \quad (10)$$

where $\sigma_{8,AGN}$ and $\sigma_{8,DM}$ is the rms fluctuations of the AGN and dark matter density distribution within spheres of a comoving radius of $8 h^{-1} \text{Mpc}$, respectively. $\sigma_{8,AGN}$ is given by

$$\sigma_{8,AGN} = J_2(\gamma)^{1/2} \left(\frac{r_{AA}}{8}\right)^{\gamma/2}, \quad (11)$$

$$J_2(\gamma) = \frac{72}{(3-\gamma)(4-\gamma)(6-\gamma)2^\gamma}, \quad (12)$$

and $\sigma_{8,DM}$ is

$$\sigma_{8,DM} = \sigma_8 \frac{D(z)}{D(0)}, \quad (13)$$

where $D(z)$ is the linear growth factor given as,

$$D(z) = \frac{5\Omega_m E(z)}{2} \int_z^\infty \frac{1+y}{E^3(y)} dy, \quad (14)$$

$$E(z)^2 = \Omega_m(1+z)^3 + \Omega_\Lambda \quad (15)$$

Using Equations (10), (11) and (13), bias is calculated from the AGN autocorrelation length as:

$$b = \left(\frac{r_{AA}}{8}\right)^{\gamma/2} J_2(\gamma)^{1/2} \left(\frac{\sigma_8 D(z)}{D(0)}\right)^{-1} \quad (16)$$

3.3 Red galaxy fraction and luminosity distribution

Using the UKIDSS/SDSS merged catalog obtained as described in section 2.2, color of each galaxy was calculated by performing SED fitting. The SED fitting was performed by using EAZY software developed by Brammer et al. (2008). As we are interested only in the galaxies associated with the AGNs, the redshift was fixed to the AGN redshift in the SED fitting. Photometric redshift was not used since the expected error can be large and does not improve the statistics significantly. It might also be possible that photo- z is not accurately determined for blue galaxies since the photo- z is mainly determined by the structure at 4000 Å, so this can produce systematic bias for selecting red galaxies preferentially. Instead of using the photometric redshift, we adapted filtering based on χ^2 of the SED fitting to select galaxies located at AGN redshifts inclusively.

A color estimator $D_{\text{opt-IR}}$ is defined as

$$D_{\text{opt-IR}} = m_{\text{opt}} - m_{\text{IR}}, \quad (17)$$

where m_{opt} and m_{IR} are magnitudes at wavelength range 3,000–3,500 Å and 10,000–12,000 Å in the rest frame, respectively. In this analysis, we used only the galaxy samples which were detected both in UKIDSS and SDSS and for which the reduced χ^2 of the SED fitting is less than a given limit.

The $D_{\text{opt-IR}}$ distribution for galaxies associated with the AGNs can be derived by the subtraction method. $D_{\text{opt-IR}}$ distributions averaged over every AGNs in a group are calculated at a central and an offset region of AGN field. We defined the central region as the region within 1 Mpc from the AGN, and defined the offset region as an annulus region at a distance of 3 to 5 Mpc. Since most of the galaxy samples at the offset region are located at redshifts different from those of AGNs, it can be regarded as background galaxies. By subtracting distribution at offset region from that at central region, we can obtain the $D_{\text{opt-IR}}$ distribution for galaxies associated with the AGNs.

The reduced χ^2 of the SED fitting for galaxies at the offset region tends to be larger than that of galaxies at the central region, since the fitting is performed by assuming incorrect redshifts. We determined the limit of the reduced χ^2 for selecting galaxies, by comparing the distributions for central and offset galaxies. We set the limit to 4.5 for $z < 0.6$, and 2.0 for $z \geq 0.6$.

In Figure 5, we show the distribution of $D_{\text{opt-IR}}$ derived

from all the AGN samples. The bimodality of galaxy color distribution is clearly seen. In the same figure, the color distributions for blue and red galaxies are deconvolved by assuming normal distribution. The peak values of the color distribution for blue and red galaxies are 3.1 and 4.2, respectively. We derive the red galaxy fraction for each AGN group by fitting the color distribution to a model function given with a sum of two normal distributions.

The luminosity distribution can be derived with the same method as that used for the color distribution described above. The absolute magnitude was calculated by $m_{\text{IR}} - DM(z)$, where $DM(z)$ is the distance modulus at redshift z . In Figure 6, we show the color-magnitude diagram obtained for all the AGN samples by the subtraction method. The red sequence and blue cloud are clearly seen. Red sequence galaxies are concentrated in a upper right region ($M < -20$ and $D_{\text{opt-IR}} > 3.5$), while blue cloud galaxies are widely spread in the dimmer part.

4 Results

4.1 Cross-correlation

All the AGN samples are divided into 12 redshift-mass groups as shown in Figure 2. Redshift is divided into three ranges 0.1–0.3, 0.3–0.6 and 0.6–1.0. We designate them as z_1 , z_2 , and z_3 , respectively. BH mass is divided into four ranges $\log(M_{\text{BH}}/M_\odot) = 6.5\text{--}7.5$, $7.5\text{--}8.2$, $8.2\text{--}9.0$, $9.0\text{--}10.0$, and they are designated as M65, M75, M82, and M90, respectively. Hereafter we call, for an example, a group of redshift range of 0.1–0.3 and mass range of 6.5–7.5 as M65- z_1 .

The results obtained by fitting the model function of Equation (7) to the observed average number densities are summarized in the first part of Table 1. In Figure 7, the cross-correlation length r_0 obtained for each redshift-mass group is plotted as a function of M_{BH} . The result shows that there is a tendency that r_0 increases with M_{BH} , while there is no clear redshift dependence.

As no clear redshift dependence is seen, the AGN samples are combined for the same mass and all the redshift groups to reduce the uncertainty resulting from intrinsic variance of clustering around each AGN, then r_0 is calculated for the combined mass groups. The projected number densities for these samples and fitted model functions are shown in Figure 8. The horizontal dashed lines in these figures correspond to n_{bg} obtained from the fitting. The projected cross-correlation functions calculated from equation (6) are shown in Figure 9, and are well expressed by a power law function.

The cross-correlation lengths derived from the fitting are plotted in Figure 10. The error bars include statistical error, systematic error, and uncertainty related with the intrinsic variance among AGNs. The uncertainty due to the intrinsic variance was estimated from a difference between the cross corre-

lation lengths calculated for two independent sub samples. The sub samples were constructed by dividing the original AGN samples into two groups in random. We generated 21 sets of two half-sized samples, calculated absolute differences of cross correlation lengths between the two sub samples $\delta r_{0,1/2}$ for each set, and selected median of $\delta r_{0,1/2}$ as an estimate of the standard deviation for the half-sized sub sample. The corresponding error on r_0 of the original sample was calculated as $\sigma_{r_0} = \delta r_{0,1/2}/\sqrt{2}$, which is summarized in Table 2.

The difference of r_0 between M75 and M90 groups is about 2.6 sigma excluding the systematic errors. For comparison the results obtained in the previous work (Komiya et al. 2013) are also plotted in the figure. They are consistent with the results of this work.

The AGN linear bias is estimated from the cross-correlation length assuming that the autocorrelation function of the galaxies is expressed by a linear combination of autocorrelation functions of three types of galaxies.

Zehavi et al. (2011) measured an autocorrelation function of galaxies up to redshift of 0.25, and derived its color and luminosity dependence. Their results show that the autocorrelation function significantly different among blue, red, and the brightest galaxies. Referring to their results, we used autocorrelation functions of the form $\xi_{\text{GG,blue}}(r) = (r/3.6h^{-1}\text{Mpc})^{-1.7}$, $\xi_{\text{GG,red}}(r) = (r/6.6h^{-1}\text{Mpc})^{-1.9}$, and $\xi_{\text{GG,bright}}(r) = (r/10.7h^{-1}\text{Mpc})^{-1.9}$ for blue and red galaxies with absolute brightness in r band $M_r \geq -22$, and the brightest galaxies with $M_r < -22$, respectively. The parameter values adapted for blue and red galaxies are the ones obtained for galaxies with $-20 < M_r < -19$. Although the absolute magnitude of our galaxy samples ranges over $-23 < M_r < -17$, we ignore the luminosity dependence in the range of $-22 < M_r < -17$ as their measured dependence is small. For galaxies with brighter than $M_r = -22$ significant increase in autocorrelation function was observed, so we used a separate function for those galaxies. We also assume that the autocorrelation functions are unchanged at redshifts up to 1.0.

To derive weighting factors among these three components, fractions of blue and red galaxies with $M_r \geq -22$ and of galaxies with $M_r < -22$ are measured by the subtraction method described in section 3.3. The obtained fractions are summarized in Table 2.

Using the autocorrelation function of galaxies derived from a linear combination of those for three galaxy types, we obtained $b = 1.52_{-0.54}^{+0.66}$, $1.47_{-0.38}^{+0.49}$, $2.38_{-0.49}^{+0.74}$, $3.08_{-0.81}^{+1.23}$ for mass group M65, M75, M82 and M90, respectively. The detailed method for deriving the AGN bias is described in section 3.2. These results are summarized in Table 2 and plotted in Figure 11. The uncertainty of b includes statistical error, systematic error corresponding to the uncertainty of ρ_0 estimation, and the intrinsic variance of the clustering around each AGN.

As is inferred from the mass-redshift distribution shown in Figure 2, even for the same redshift group the higher mass groups tends to be biased to higher redshift. To reduce the redshift bias, we constructed redshift matched samples for each redshift group. The redshift matched samples were constructed by selecting the same number of AGN samples for each redshift bin with 0.02 width.

The number of samples selected in this way is reduced significantly from the original samples, so the intrinsic fluctuation of clustering strength of each sample can introduce large scatter to the cross-correlation length. To obtain the most typical sample in term of clustering, we randomly constructed 21 sets of redshift matched sample for each redshift group, calculated cross-correlation length for each sample set, and selected a sample set for which cross-correlation length was median among the sample sets. The result is shown in Figure 12 and summarized in the middle part of Table 1. The tendency of increase in r_0 as a function M_{BH} is seen in the redshift matched samples as well.

To see the redshift dependence of r_0 for the same M_{BH} , we constructed mass matched samples in the same way as used to construct redshift matched samples with 0.2 dex of bin width of mass histogram. The results are shown in Figure 13 and summarized in the last part of Table 1. No clear redshift dependence is seen for any mass group.

These results are consistent with our previous result in Komiya et al. (2013), although we have used the most recent UKIDSS catalog and slightly different data selection criteria and mass correction.

4.2 Properties of Galaxies

To investigate the properties of galaxies at environment of AGNs with the most massive SMBHs, where increase of clustering is found, we calculated the color parameter $D_{\text{opt-IR}}$ for all the detected galaxies and derived its distributions for galaxies associated with the AGNs by using the subtraction method described in section 3.3. $D_{\text{opt-IR}}$ parameter corresponds to the color defined as difference in brightness between the wavelength ranges of 3,000–3,500 Å and 10,000–12,000 Å in the rest frame. In Figure 14 we show $D_{\text{opt-IR}}$ parameter distributions for each redshift and mass sample. The observed distributions are fitted with a two component model (red and blue galaxy components) assuming the normal distribution for both components. The mean and standard deviation of the distribution of each component are fixed to the predetermined values, and only the mixing ratio and the normalization constant are taken as free parameters. The predetermined values of the mean and standard deviation are obtained by fitting the model function to the observed distribution for all the AGN samples with taking all the parameters free. The parameter values obtained from this fitting

are summarized in Table 3.

The fractions of red galaxies are plotted in the left panel of Figure 15 as a function of M_{BH} . The normalized excess densities ω' , which are defined as $\omega' = (n_{\text{on}} - n_{\text{off}})/\rho_0$, are plotted in the right panel of the figure. n_{on} and n_{off} are the surface number density of galaxies at projected distance of 0–1Mpc (on region) and 3–5Mpc (off region) from AGN, respectively. The ω' can be considered as an approximate estimate of the projected cross-correlation function. The error bars represent one sigma Poisson statistical error for both figures. Since red galaxies are typically brighter than blue galaxies as seen in Figure 6, the observed red galaxy fraction tends to be higher for the higher redshift samples. Thus, the comparison of the red galaxy fraction is meaningful only for the same redshift samples.

At redshift z1, both of the red galaxy fraction and the normalized excess density are almost unchanged among the mass groups of M65, M75 and M82. At redshift z2, significant increase of the normalized excess density is seen for the red galaxies of the mass group M90. At redshift z3, blue galaxies are hardly detected and red fraction is $\sim 100\%$ for mass groups M82 and M90.

The data samples used in Figures 14 and 15 have a slight difference in the redshift distribution among the respective mass groups even for the same redshift groups; the lower mass group has relatively smaller redshift than the higher mass group. The red fraction of the higher mass group, therefore, can be biased to higher value. To reduce the effect of redshift bias, the same analysis was performed also for the redshift matched samples.

The distributions of $D_{\text{opt-IR}}$ for the redshift matched samples are shown in Figure 16. Since the statistics of lower mass groups are poor, the two lower mass groups are combined. The obtained red galaxy fractions and normalized excess density are plotted as a function of M_{BH} in Figure 17. These results also show that red galaxy becomes the dominant component in the highest mass group, M90.

To see the relative difference of luminosity function of galaxies around SMBHs with lower and higher mass, absolute magnitude distributions are compared in Figure 18. They are obtained by using the subtraction method described in section 3.3. In this comparison, redshift matched samples are used so that both of the samples have the same sensitivity on the detection of galaxies. To check the equivalence among the samples in term of the sensitivity of observations, the distributions of ρ_0 are compared in Figure 19. We found that they are consistent with each other.

The left panel of Figure 18 shows the comparison between the AGN groups of M65+M75 and M82 for redshift range of z1, and the ratio (high mass/low mass) of the magnitude distributions is shown in the bottom of the panel. Since the lower mass samples has smaller excess density than the higher mass sample, we combined two lower mass samples to increase the statistics. The red histogram is the distribution of absolute mag-

nitude for higher mass sample, and the blue histogram is for lower mass sample. The absolute magnitude is estimated at wavelength range of 1–1.2 μm in the rest frame by fitting model SED to the observed one using the EAZY code as described in section 3.3. The ratio is peaked around -20.25 mag, and it shows a steep decline at dimmer side. The significance of the depletion of galaxies in the M82-z1 group against (M65+M75)-z1 is ~ 2.5 sigma at magnitude range from -19.5 to -18.0 mag. The dashed line on the ratio plot is a power law function fitted to the observations at brighter side below -20.0 mag. The best fit value of the power law index is -0.096 ± 0.075 for the ratio between M82-z1 and (M65+M75)-z1 samples.

The same comparison between the mass groups M75+M82 and M90 at redshift z2 and z3 is shown in the right panel of Figure 18. The observed ratio is fitted with the power law function and the power law index is estimated to be $+0.046 \pm 0.093$, which is consistent with a constant over the luminosity range. The ratio of M82 and M65+M75 at redshift z1 and that of M90 and M75+M82 at redshift z2 and z3 are compared in Figure 20.

5 Discussion

We have successfully reconfirmed the increase of cross-correlation length above $M_{\text{BH}} = 10^{8.2} M_{\odot}$ (Figure 10), that was already reported in the previous paper by Komiya et al. (2013), by adapting the improved data selection and using the most recent UKIDSS DR9 dataset. We also confirmed that the trend is also seen in the redshift matched samples (Figure 12), and the cross-correlation length does not depend on the redshift (Figure 13). Although the AGN luminosity dependence was not investigated in this paper, the previous work reported no significant dependence on the luminosity (Komiya et al. 2013).

The derived AGN bias b (Figure 11) increase with M_{BH} above $10^{8.2} M_{\odot}$. The AGN bias for M75 mass group is $b = 1.47_{-0.38}^{+0.49}$ at average redshift of 0.47, which is consistent with those of SDSS QSOs by Ross et al. (2009), 2dF QSOs by Croom et al. (2005), X-ray selected AGNs by Hickox et al. (2009), and optically selected AGNs by Krumpke et al. (2012).

The AGN bias of mass group M90 is estimated to be $b = 3.08_{-0.81}^{+1.23}$, which is larger than that of radio AGNs of Hickox et al. (2009) by one sigma and indicates that those AGNs reside in haloes with mass larger than $10^{13.5} h^{-1} M_{\odot}$.

Shen et al. (2009) also studied virial mass dependence of clustering strength using SDSS QSOs at redshift range from 0.4 to 2.5. They found that the difference in the clustering strength for the 10% most massive QSOs and the remaining 90% is significant at the $\sim 2\sigma$ level. They also studied radio activity dependence of clustering by comparing between the radio-loud and radio-quiet QSOs samples, and found that the radio-loud QSOs are more strongly clustered than the radio-quiet QSOs at the $\sim 2.5\sigma$ level. Although these radio-loud QSOs tend to have

systematically larger BH masses than those radio-quiet QSOs by 0.12 dex, the difference in their clustering remains when the comparison is made for mass matched samples. Thus they argue that more massive host halos, and denser environments may be related to the triggering of radio activity.

Mandelbaum et al. (2009) also found that the radio AGNs are hosted by dark matter halo with $\sim 1.6 \times 10^{13} h^{-1} M_{\odot}$. There are observational evidences that radio-loud AGNs are associated with the massive galaxies (Best et al. 2005) and have SMBHs with masses typically larger than $10^9 M_{\odot}$ (Laor 2000). Ishibashi et al. (2014) also claimed that radio galaxies are preferentially associated with the more massive black holes.

According to the theoretical predictions by Fanidakis et al. (2011) for radio loudness and black holes mass (see bottom panel of Figure 14 in their paper), AGNs in the hot halo mode are distributed at a region of higher radio-loudness and their black hole mass extends from $10^6 M_{\odot}$ up to $10^{10} M_{\odot}$, while the AGNs in the cold accretion mode are at lower part in radio-loudness and their black hole mass is limited below $\sim 10^{8.6} M_{\odot}$. It is, therefore, expected that AGNs in the hot halo mode, i.e. in dark matter haloes with higher mass, can preferentially be selected by higher radio-loudness or higher black hole mass. Thus the increasing trend of AGN bias at higher black hole masses found in this work are consistent with those results obtained by the other authors, and they all are also consistent with the picture drawn from Fanidakis et al. (2011).

The main purpose of this paper is to investigate what type of galaxy contributes to the increase of galaxy density around the most massive SMBH. In this work we considered two kind of galaxy types which are classified based on the distribution in a color-magnitude diagram. One is a blue cloud galaxy (blue galaxy) which occupies a bluer and dimmer side of the distribution, and the other is a red sequence galaxy (red galaxy) which has a redder and narrower distribution in the color-magnitude diagram (Figure 6).

It should be noticed that detection efficiency for blue galaxy decreases more rapidly with increasing redshift than for red galaxy due to the difference in their brightness. As is shown in the bottom panels of Figure 14, at redshift range of $z3$ ($z=0.6-1.0$) the observed fraction of blue galaxies is very low, this is largely because most of the blue galaxies are below the detection limit. At redshift range of $z2$ ($z=0.3-0.6$) the fraction of the detected blue galaxy constitutes about 20% of all the detected galaxies, while at redshift range of $z1$ ($z=0.1-0.3$) the fraction increase to around 40%. As shown here, the observed red/blue fraction has strong redshift dependence and should not be compared between different redshift groups.

The results of the two component analysis on the $D_{\text{opt-IR}}$ distribution (Figures 14,15) indicate that the increase of clustering strength found in the cross-correlation analysis for the most massive mass group M90 relative to the lower mass groups are

mainly due to the contribution of red galaxies. This can be justified from the observational evidence that increase of the normalized excess density at the transition from M82 to M90 for redshift $z2$ is significant for red galaxies, while it is almost unchanged or rather decreasing for blue galaxies. It is known that early type galaxies tend to be found at a high density region such as a cluster/group core (Dressler 1980; Postman & Geller 1984; Balogh et al. 2004). It is, therefore, naturally expected that the high density around the high mass SMBH is coupled with early type galaxies.

The other indication from this analysis is that the increase of the clustering strength found in the cross-correlation analysis for M82 relative to the M75 is due to the contribution from both of the red and blue galaxies. The red fraction is almost unchanged between M82 and M75, and slight increase in the normalized excess density from M75 to M82 is seen in both of the red and blue components for redshift groups $z1$ and $z2$.

The same analysis is performed also for the redshift matched samples (Figure 16 and 17). The trend of the increase in the red fraction and normalized excess density for red galaxies of the most massive group (M90) is also seen in this result. The comparison between M82 and M65+M75 at redshift $z1$ shows that increase in the normalized excess density are seen in both the red and blue galaxies.

Two physical mechanisms could be relevant to this evolution. One is related with the increase of brightness of blue dim galaxies induced by starburst triggered in a secular and merger mode, which can result in the increase of the detectable galaxy density. Another one is related with the transition from blue to red galaxies, which can be the result of a feedback or gas removal mechanism shutting off the star burst activity. The latter process may follows the former process. In case where there is an enough time delay between the both processes, we could observe the increase of density both for red and blue galaxies as is the case of M82 group. If the time delay is short, only the increase of red galaxy density will be observed, and this could be the case of M90 group. The evolution of properties of galaxies around AGNs observed in this work could be explained in this manner.

According to the theoretical works by Fanidakis et al. (2013), the hot halo mode can be the most effective accretion mechanism in massive haloes with $M_h > 10^{12.5} M_{\odot}$. In such a massive halo most of the galaxies are expected to be in red sequence since AGN feedback shut off the gas cooling and star formation in their model. In galaxies turned into red sequence, i.e. early type galaxies, gas accretion from the evolving stars to the center of SMBH could also occur as claimed by Ciotti & Ostriker (2001). Considering these theoretical predictions, the dominance of red galaxies around AGNs with higher BH mass obtained in this work is indicative of predominance of hot halo mode and/or gas accretion from evolving stars for the growth of

the most massive SMBHs.

The Eddington ratios of our AGN samples in M90-z1 group are distributed in the range $\lambda = 0.003 - 0.1$, and peaked around $\log(\lambda) \sim -1.8$. The lower bound of the distribution is limited by the detection limit, so the intrinsic peak can be expected to be much lower than $\log(\lambda) = -2$. The bolometric luminosity of the same samples is above 10^{45} erg/s. According to the model of Fanidakis et al. (2013b) for those bolometric luminosity, two branches exist in the $M_{\text{halo}}-L_{\text{bol}}$ diagram (see Figure 1 in their paper); one is the branch of starburst mode for AGNs in dark matter halo of $10^{12} M_{\odot}$, the other is the branch of hot halo mode for AGNs in dark matter halo of $10^{15} M_{\odot}$. Considering that the Eddington ratios of our samples are lower than those expected for the starburst mode (~ 0.1), the sample of M90-z1 are consistent with the AGNs in the branch of hot halo mode.

We also investigated relative difference of luminosity function between the low and high mass groups. The redshift matched samples are used for making them directly comparable with each other. The equivalence among the samples in term of the sensitivity of observations was checked by comparing the distributions of ρ_0 (Figure 19), and we found that they are consistent with each other. Thus the distributions of completeness fraction are the same for the redshift matched samples, and the completeness fraction can be canceled by calculating the ratio.

For the redshift range z1, comparison between the M82 mass sample and the lower mass sample, which is a combined sample of M65+M75, is made in the left panel of Figure 18. The figure indicates that an increase of galaxy density for the higher mass sample would be caused by galaxies brighter than $M_{\text{IR}} = -19.5$ mag. At a dimmer side of $M_{\text{IR}} > -19.5$ mag, on the other hand, the luminosity function of the higher mass sample is smaller than that of the smaller mass group. The significance of the deficit of galaxies for the higher mass sample relative to the smaller mass sample is 2.5 sigma at absolute brightness range from -19.5 to -18.0 mag.

Considering that blue galaxies dominate the dimmer side of the luminosity function, the difference of the luminosity functions could be the result of brightening of the dim blue galaxies in the transition from lower mass group (M65+M75) to higher mass group (M82). Besides, to make the red/blue galaxy ratio unchanged some but not all of the blue galaxies are need to be transformed to red galaxies.

The plot of the ratio between luminosity function of M82 and M65+M75 shows that the increase fraction is larger at the dimmer side and peaked around $M_{\text{IR}} = -20.5$ mag, and it is approximately fitted with a power law function with the power index of -0.096 ± 0.075 . This may indicate that the dimmer galaxies have higher probability to increase their brightness by interaction and/or major/minor merger.

For the redshift ranges z2 and z3, a comparison between the M90 and M75+M82 groups is made in the right panel of

Figure 18, which shows the ratio of the luminosity functions is almost constant at $M_{\text{IR}} < -20$ mag. If the brightening of blue galaxies occurs at a same rate between the two groups, the difference is only the rate of blue to red transformation, and the transformation occurs without much affecting the brightness in the 1-1.2 Å band, the constant ratio of the luminosity functions is naturally expected.

6 Conclusions

In this paper, using the updated UKIDSS catalog we have successfully reconfirmed the previous findings of Komiya et al. (2013) that the clustering of galaxies around AGNs with the most massive SMBH is larger than those with less massive SMBH. The AGN bias was derived for each BH mass group. The obtained AGN bias are $b = 1.52^{+0.66}_{-0.54}$, $1.47^{+0.49}_{-0.38}$, $2.38^{+0.74}_{-0.49}$, $3.08^{+1.23}_{-0.81}$ for mass group M65, M75, M82 and M90, respectively. We further investigated what type of galaxies are associated in the environment of the most massive SMBH to reveal the nature of evolution mechanism of SMBHs and galaxies. As a result, it is found that red galaxies are dominated around AGNs with the most massive SMBH. The red galaxy fraction increases from 0.73 ± 0.04 for M82 mass group to 0.98 ± 0.07 for M90 at redshift z2. This is the first observational result that revealed the nature of galaxies at such environments from more than thousands of AGN samples. We also compared, for the first time, luminosity functions of galaxies at environments of AGNs with lower and higher mass SMBH, and found that there is an indication that shows brightening of dim and blue galaxies along with the evolution of SMBHs. Summarizing the results obtained in this work, we can deduce the following scenario on the evolution of SMBH and its environment galaxies as a function of M_{BH} .

Below the critical mass around $10^{8.2} M_{\odot}$, the environment of SMBH does not depend on M_{BH} and is almost equivalent to that of a quiescent galaxy. At that environment, the fraction of blue galaxy is more than 40%. Secular evolution can be the main driver for the evolution of these SMBHs. Above the critical mass, dim and blue galaxies increase its brightness, which is presumably caused via starburst. Some of the brightened blue galaxies are transformed to red galaxies after the AGN feedback or some other mechanisms which shut off star formation in the galaxies operates.

In the environment of AGNs of M82 mass group, increases in densities for both blue and red galaxies are observed, while in the environment of AGNs of M90 mass group, the increase is seen only for the red galaxies. This difference may be due to the difference of time lag between the starburst and some mechanism to shut off the starburst activity.

Considering that there is a correlation between the transition in properties of environmental galaxies and mass evolution of

SMBHs above $M_{\text{BH}} = 10^{8.2} M_{\odot}$, they are governed by a sort of environmental effect rather than internal secular evolution. This transition makes galaxies observable by pushing up the brightness above the detection limit, and results in the increase of observed galaxy number density and the clustering length.

The hot halo mode as well as gas accretion from evolving stars may be one of the most dominant mechanism in the growth of the most massive SMBHs, as inferred from properties of environment galaxies.

Acknowledgments

We would like to thank the anonymous referee for his/her helpful comments. Results are based on data obtained from the Japanese Virtual Observatory, which is operated by the Astronomy Data Center, National Astronomical Observatory of Japan. Funding for SDSS-III has been provided by the Alfred P. Sloan Foundation, the Participating Institutions, the National Science Foundation, and the U.S. Department of Energy Office of Science. The SDSS-III web site is <http://www.sdss3.org/>. SDSS-III is managed by the Astrophysical Research Consortium for the Participating Institutions of the SDSS-III Collaboration including the University of Arizona, the Brazilian Participation Group, Brookhaven National Laboratory, Carnegie Mellon University, University of Florida, the French Participation Group, the German Participation Group, Harvard University, the Instituto de Astrofísica de Canarias, the Michigan State/Notre Dame/JINA Participation Group, Johns Hopkins University, Lawrence Berkeley National Laboratory, Max Planck Institute for Astrophysics, Max Planck Institute for Extraterrestrial Physics, New Mexico State University, New York University, Ohio State University, Pennsylvania State University, University of Portsmouth, Princeton University, the Spanish Participation Group, University of Tokyo, University of Utah, Vanderbilt University, University of Virginia, University of Washington, and Yale University. This work is based in part on data obtained as part of the UKIRT Infrared Deep Sky Survey.

References

- Aihara, H. et al. 2011, *ApJS*, 193, 29
 Alexander, D. M., et al. 2012, *New Astronomy Reviews*, 56, 93
 Alleato, V., et al. 2011, *ApJ*, 736, 99
 Balogh, M. L., et al. 2004, *ApJ*, 615, L101
 Best, P. N., et al. 2005, *MNRAS*, 362, 25
 Boyle, B. J., Terlevich, R. J. 1998, *MNRAS*, 293, L49
 Brammer, G. B., van Dokkum, P. G., Coppi, P. 2008, *ApJ*, 686, 1503
 Bradshaw, E. J., et al. 2011, *MNRAS*, 415, 2626
 Ciotti, L., Ostriker, J. P. 2001, *ApJ*, 551, 131
 Ciotti, L., Ostriker, J. P. 2007, *ApJ*, 665, 1038
 Cisternas, M. et al., 2011, *ApJ*, 726, 57
 Coil, A. L., et al. 2009, *ApJ*, 701, 1484
 Croom, S. M., et al. 2005, *MNRAS*, 356, 415
 Croton D. J. et al., 2006, *MNRAS*, 365, 11
 Donoso, E., Li, Cheng, Kauffmann, G., Best, P. N. and Heckman, T. M. 2010, *MNRAS*, 407, 1078
 Dressler, A. 1980, *ApJ*, 236, 351
 Fanidakis, N. et al., 2011, *MNRAS*, 410, 53
 Fanidakis, N. et al., 2013, *MNRAS*, 435, 679
 Fanidakis, N. et al., 2013b, *MNRAS*, 436, 315
 Ferrarese, L., Merritt, D. 2000, *ApJ*, 539, L9
 Gebhardt, K., et al. 2000, *ApJ*, 539, L13
 Georgakakis, A., et al. 2014, *MNRAS*, 443, 3327
 Greene, J. E. & Ho, L. C., 2007, *ApJ*, 667, 131
 Greene, J. E. & Ho, L. C., 2007, *ApJ*, 670, 92
 Hickox, R. C., et al., 2009, *ApJ*, 696, 891
 Hickox, R. C., et al. 2011, *ApJ*, 731, 117
 Ho, L. C. 2007, *ApJ*, 668, 94
 Hopkins, P. F., Hernquist, L., Cox, T. J., Keres, D. 2008, *ApJS*, 175, 356
 Ishibashi, W., Auger, M. W., Zhang, D., & Fabian, A. C. 2014, *MNRAS*, 443, 1339
 Kauffmann, G., Heckman, T. M. 2009, *MNRAS*, 397, 135
 Kaviraj, S. 2014, *MNRAS*, 440, 2944
 Keres, D., et al., 2009, *MNRAS*, 395, 160
 King, A., 2014, *Space Science Reviews*, 183, 427
 Komiyama, Y., Shirasaki, Y., Ohishi, M., Mizumoto, Y., 2013, *ApJ*, 775, 43
 Kormendy, J. & Ho, Kennicutt, R. C., Jr. 2004, *ARA&A*, 42, 603
 Kormendy, J. & Ho, L. C. 2013, *ARA&A*, 51, 511
 Koutoulidis, L. et al. 2013, *MNRAS*, 428, 1382
 Krumpel, M., Miyaji, T., Coil, A. L., and Aceves, H. 2012, *ApJ*, 746, 1
 Lagos, C. D. P., Cora, S. A., and Padilla, N. D. 2008, *MNRAS*, 388, 587
 Laor, A. 2000, *ApJ*, 543, L111
 Lawrence, A. et al. 2007, *MNRAS*, 379, 1599
 Longair, M. S. and Seldner, M. 1979, *MNRAS*, 189, 433
 Madau, P., Ferguson, H. C., Dickinson, M. E., Giavalisco, M., Steidel, C. C., & Fruchter, A. 1996, *MNRAS*, 283, 1388
 Magorrian, J., et al. 1998, *AJ*, 115, 2285
 Mandelbaum, R., Li, C., Kauffmann, G., White, S. D. M. 2009, *MNRAS*, 393, 377
 Mountrichas, G., et al. 2013, *MNRAS*, 430, 661
 Pentericci, L., et al. 2013, *A&A*, 552, A111
 Postman, M., Geller, M. J. 1984, *ApJ*, 281, 95
 Richstone, D., et al. 1998, *Nature*, 395, A14
 Ross, N. P., et al. 2009, *ApJ*, 697, 1634
 Sabater, J., Best, P. N., and Heckman, T. M. 2015, *MNRAS*, 447, 110
 Sanders, D. B., et al. 1988, *ApJ*, 325, 74
 Zhang, S., Wang, T., Wang, H., Hongyan, Z. 2013, *ApJ*, 773, 175
 Shen, Y., et al. 2009, *ApJ*, 697, 1656
 Shen, Y. et al., 2011, *ApJS*, 194, 45
 Sheth, R. K. et al. 2001, *MNRAS*, 323, 1
 Shirasaki, Y., et al. 2011, *PASJ*, 63, 469
 Silverman, J. D., et al. 2009, *ApJ*, 695, 171
 Silverman, J. D., et al. 2011, *ApJ*, 743, 2
 Treister, E., Schawinski, K, Urry, C. M., & Simmons, B. D. 2012, *ApJ*, 758, L39
 Ueda, Y., Akiyama, M., Ohta, K., & Miyaji, T. 2003, *ApJ*, 598, 886
 van den Bosch, F. C. 2002, *MNRAS*, 331, 98
 Zehavi, I., et al. 2011, *ApJ*, 736, 59
 Zheng, X. Z. et al., 2009, *ApJ*, 707, 1566

Table 1. Parameters derived from the cross-correlation analysis for each BH mass and redshift range

BH mass $\log M$	redshift	$n_{\text{AGN}}^{\text{a}}$	$\langle \log M \rangle^{\text{b}}$	$\langle z \rangle^{\text{c}}$	r_0^{d} $h^{-1} \text{Mpc}$	$\sigma_{\text{stat}}^{\text{e}}$ $h^{-1} \text{Mpc}$	$\langle n_{\text{bg}} \rangle^{\text{f}}$ Mpc^{-2}	$\langle \rho_0 \rangle^{\text{g}}$ 10^{-3}Mpc^{-3}
All samples								
6.5–7.5	0.1–1.0	524	7.2	0.24	$6.1^{+0.7}_{-0.6}$	0.34	38.85 ± 0.05	5.08 ± 0.8
	0.1–0.3	429	7.1	0.20	$6.2^{+0.7}_{-0.6}$	0.36	45.17 ± 0.06	5.61 ± 0.9
7.5–8.2	0.1–1.0	1880	7.9	0.47	$5.8^{+0.8}_{-0.6}$	0.23	15.24 ± 0.02	2.71 ± 0.5
	0.1–0.3	520	7.8	0.22	$6.3^{+0.7}_{-0.6}$	0.32	37.60 ± 0.05	5.32 ± 0.9
	0.3–0.6	804	7.9	0.45	$4.8^{+0.8}_{-0.6}$	0.35	9.41 ± 0.02	2.48 ± 0.5
	0.6–1.0	556	8.0	0.75	$5.4^{+1.6}_{-1.2}$	0.85	2.78 ± 0.01	0.61 ± 0.2
8.2–9.0	0.1–1.0	4485	8.6	0.65	$7.7^{+1.2}_{-0.8}$	0.16	6.89 ± 0.01	1.42 ± 0.3
	0.1–0.3	362	8.5	0.23	$7.7^{+0.9}_{-0.7}$	0.32	33.10 ± 0.06	5.18 ± 0.8
	0.3–0.6	1380	8.6	0.46	$7.0^{+1.0}_{-0.8}$	0.21	8.59 ± 0.02	2.29 ± 0.5
	0.6–1.0	2743	8.6	0.80	$8.7^{+2.4}_{-1.4}$	0.33	2.58 ± 0.01	0.49 ± 0.2
9.0–10.0	0.1–1.0	1170	9.2	0.72	$9.0^{+1.6}_{-1.1}$	0.34	4.79 ± 0.01	1.01 ± 0.3
	0.3–0.6	289	9.2	0.48	$8.8^{+1.4}_{-1.0}$	0.42	8.19 ± 0.04	2.17 ± 0.5
	0.6–1.0	845	9.2	0.83	$9.7^{+2.8}_{-1.7}$	0.62	2.50 ± 0.01	0.44 ± 0.2
Redshift matched samples								
6.5–7.5	0.1–0.3	298	7.1	0.22	$5.6^{+0.7}_{-0.6}$	0.44	35.04 ± 0.07	5.29 ± 0.8
7.5–8.2		298	7.8	0.22	$6.3^{+0.8}_{-0.6}$	0.41	36.23 ± 0.07	5.35 ± 0.9
8.2–9.0		298	8.5	0.22	$8.1^{+0.9}_{-0.7}$	0.34	35.96 ± 0.07	5.33 ± 0.9
7.5–8.2	0.3–0.6	289	7.9	0.48	$4.6^{+0.9}_{-0.8}$	0.65	8.47 ± 0.03	2.18 ± 0.5
8.2–9.0		289	8.6	0.48	$6.9^{+1.1}_{-0.9}$	0.49	8.25 ± 0.03	2.17 ± 0.5
9.0–10.0		289	9.2	0.48	$8.8^{+1.4}_{-1.0}$	0.42	8.19 ± 0.04	2.17 ± 0.5
7.5–8.2	0.6–1.0	483	8.0	0.76	$5.3^{+1.7}_{-1.3}$	0.97	2.73 ± 0.01	0.58 ± 0.2
8.2–9.0		483	8.6	0.76	$8.1^{+2.2}_{-1.4}$	0.72	2.67 ± 0.02	0.58 ± 0.2
9.0–10.0		483	9.2	0.77	$9.2^{+2.5}_{-1.5}$	0.68	2.76 ± 0.02	0.58 ± 0.2
Mass matched samples								
7.5–8.2	0.1–0.3	371	7.9	0.22	$6.1^{+0.7}_{-0.6}$	0.38	36.91 ± 0.06	5.30 ± 0.9
	0.3–0.6	371	7.9	0.45	$4.7^{+0.8}_{-0.7}$	0.54	9.53 ± 0.03	2.45 ± 0.5
	0.6–1.0	371	7.9	0.74	$4.4^{+1.6}_{-1.3}$	1.17	2.85 ± 0.02	0.64 ± 0.2
8.2–9.0	0.1–0.3	362	8.5	0.23	$7.7^{+0.9}_{-0.7}$	0.32	33.10 ± 0.06	5.18 ± 0.8
	0.3–0.6	362	8.5	0.46	$6.8^{+1.1}_{-0.8}$	0.42	8.54 ± 0.03	2.32 ± 0.5
	0.6–1.0	362	8.5	0.80	$7.7^{+2.3}_{-1.5}$	0.99	2.61 ± 0.02	0.50 ± 0.2
9.0–10.0	0.3–0.6	289	9.2	0.48	$8.8^{+1.4}_{-1.0}$	0.42	8.19 ± 0.04	2.17 ± 0.5
	0.6–1.0	289	9.2	0.84	$9.4^{+3.0}_{-1.9}$	1.18	2.49 ± 0.02	0.40 ± 0.2

^a number of sample AGNs.^b average of logarithm of BH mass.^c average redshift.^d correlation length, the error contains systematic error due to uncertainty of ρ_0 and 1σ statistical error.^e statistical error of r_0 .^f average of projected number density of background galaxies.^g average of the averaged number density of galaxies at the AGN redshift.**Table 2.** Parameters derived from the bias estimate

mass $\log M_{\odot}$	redshift	$f_{\text{blue}}^{\text{a}}$	$f_{\text{red}}^{\text{b}}$	$f_{\text{bright}}^{\text{c}}$	$\sigma_{r_0}^{\text{d}}$ $h^{-1} \text{Mpc}$	r_{AA}^{e} $h^{-1} \text{Mpc}$	$\gamma_{\text{AA}}^{\text{f}}$	b^{g}
6.5–7.5	0.1–1.0	0.321	0.669	0.010	1.16	$6.33^{+3.4}_{-2.5}$	1.69	$1.52^{+0.66}_{-0.54}$
7.5–8.2	0.1–1.0	0.296	0.650	0.054	0.65	$5.29^{+2.1}_{-1.6}$	1.69	$1.47^{+0.49}_{-0.38}$
8.2–9.0	0.1–1.0	0.230	0.581	0.189	0.35	$8.45^{+3.2}_{-2.0}$	1.69	$2.38^{+0.74}_{-0.49}$
9.0–10.0	0.1–1.0	0.112	0.668	0.220	0.82	$11.09^{+5.4}_{-3.4}$	1.68	$3.08^{+1.23}_{-0.81}$

^a fraction of blue galaxies with brightness $M_r \geq -22$ ^b fraction of red galaxies with brightness $M_r \geq -22$ ^c fraction of galaxies with brightness $M_r < -22$ ^d uncertainty of the cross-correlation length r_0 due to the intrinsic variance of clustering around each AGN.^e autocorrelation length of AGNs.^f power law index of AGN autocorrelation function.^g AGN bias.

Table 3. Parameters derived from the two component analysis on $D_{\text{opt-IR}}$ distributions

redshift	mass $\log M_{\odot}$	$\mu_{\text{red}}^{\text{a}}$	$\sigma_{\text{red}}^{\text{b}}$	$\mu_{\text{blue}}^{\text{c}}$	$\sigma_{\text{blue}}^{\text{d}}$	$F_{\text{red}}^{\text{e}}$	$\omega'_{\text{red}}^{\text{f}}$ 10^2Mpc	$\omega'_{\text{blue}}^{\text{g}}$ 10^2Mpc
<i>All samples</i>								
0.1–1.0	6.5–10.0	4.17 ± 0.05	0.41 ± 0.03	3.06 ± 0.23	0.50 ± 0.13	0.77 ± 0.09		
0.1–0.3	6.5–7.5	4.17	0.41	3.06	0.50	0.66 ± 0.06	0.64 ± 0.09	0.32 ± 0.06
	7.5–8.2	4.17	0.41	3.06	0.50	0.66 ± 0.05	0.60 ± 0.07	0.31 ± 0.05
	8.2–9.0	4.17	0.41	3.06	0.50	0.66 ± 0.05	0.73 ± 0.08	0.37 ± 0.06
0.3–0.6	7.5–8.2	4.17	0.41	3.06	0.50	0.84 ± 0.10	0.43 ± 0.08	0.08 ± 0.06
	8.2–9.0	4.17	0.41	3.06	0.50	0.73 ± 0.04	0.67 ± 0.06	0.25 ± 0.05
	9.0–10.0	4.17	0.41	3.06	0.50	0.98 ± 0.07	1.37 ± 0.15	0.22 ± 0.10
0.6–1.0	7.5–8.2	4.17	0.41	3.06	0.50	0.81 ± 0.30	0.40 ± 0.17	0.09 ± 0.17
	8.2–9.0	4.17	0.41	3.06	0.50	1.00 ± 0.08	1.28 ± 0.09	0.00 ± 0.10
	9.0–10.0	4.17	0.41	3.06	0.50	1.00 ± 0.14	1.39 ± 0.17	0.00 ± 0.19
<i>Redshift matched samples</i>								
0.1–0.3	6.5–8.2	4.17	0.41	3.06	0.50	0.64 ± 0.04	0.73 ± 0.07	0.41 ± 0.05
	8.2–10.0	4.17	0.41	3.06	0.50	0.66 ± 0.05	0.92 ± 0.10	0.48 ± 0.08
0.3–0.6	7.5–9.0	4.17	0.41	3.06	0.50	0.59 ± 0.09	0.41 ± 0.10	0.28 ± 0.07
	9.0–10.0	4.17	0.41	3.06	0.50	0.98 ± 0.07	1.37 ± 0.15	0.02 ± 0.10
0.6–1.0	7.5–9.0	4.17	0.41	3.06	0.50	0.86 ± 0.16	0.65 ± 0.14	0.11 ± 0.14
	9.0–10.0	4.17	0.41	3.06	0.50	1.00 ± 0.13	1.50 ± 0.20	0.00 ± 0.19

^amean of the $D_{\text{opt-IR}}$ distribution for red component.

^bstandard deviation of the $D_{\text{opt-IR}}$ distribution for red component.

^cmean of the $D_{\text{opt-IR}}$ distribution for blue component.

^dstandard deviation of the $D_{\text{opt-IR}}$ distribution for blue component.

^efraction of red component.

^fnormalized excess density for red component.

^gnormalized excess density for blue component.

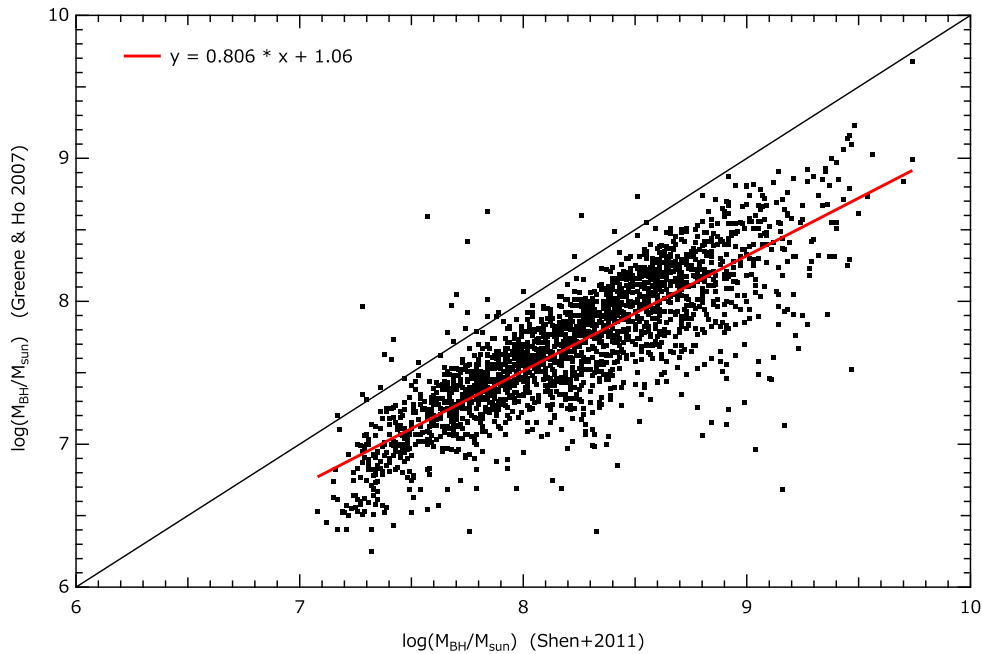


Fig. 1. Comparison of black hole masses derived by Shen et al. (2011) (horizontal axis) and Greene et al. (2007a) (vertical axis). The solid red line represents a linear function fitted to the data points.

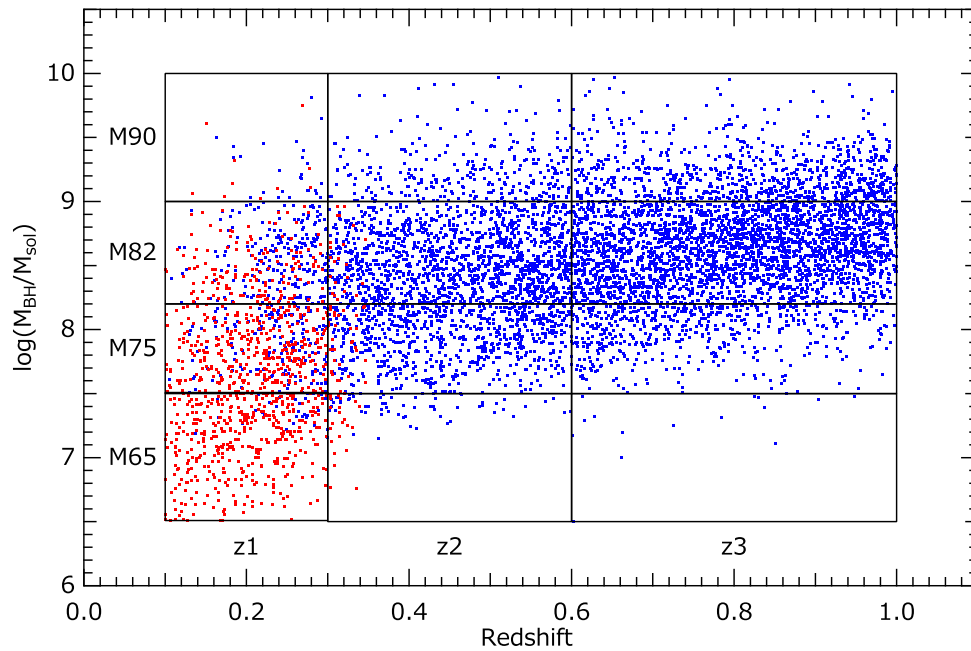


Fig. 2. Distribution of redshift and BH mass of AGNs. AGNs from Greene et al. (2007a) and Shen et al. (2011) are plotted in red and blue colors, respectively. The mass correction is applied to AGNs of Greene et al. (2007a) to compensate the systematic difference between the two catalogs.

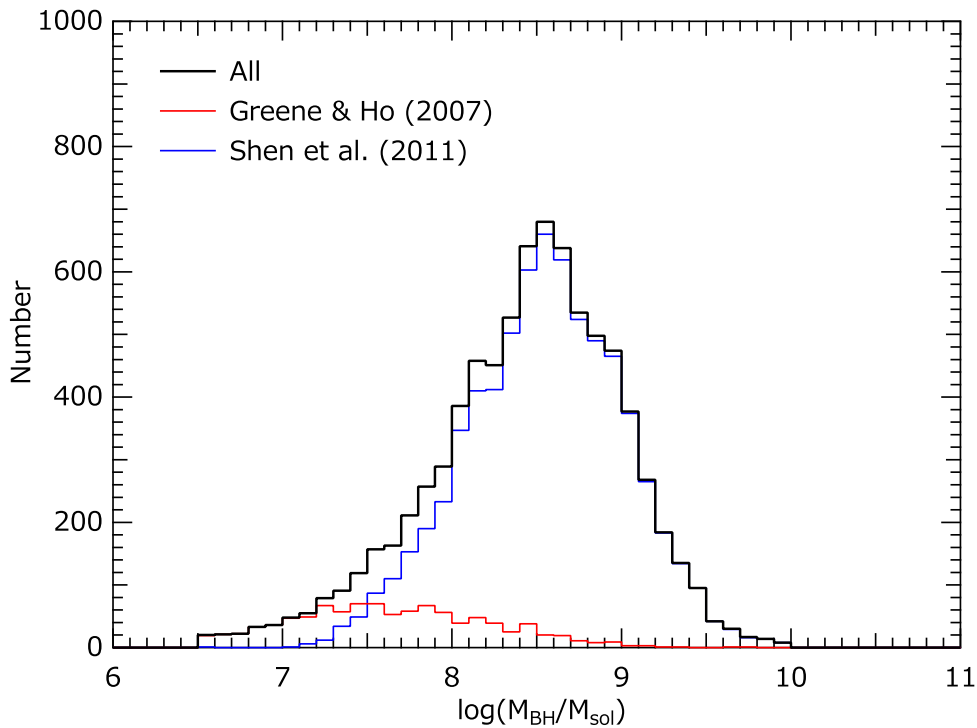


Fig. 3. Distribution of BH mass for the same sample as shown in Figure 2. The red histogram with smaller masses is for Greene et al. (2007a), the blue one is for Shen et al. (2011). The sum of them is shown with the black histogram.

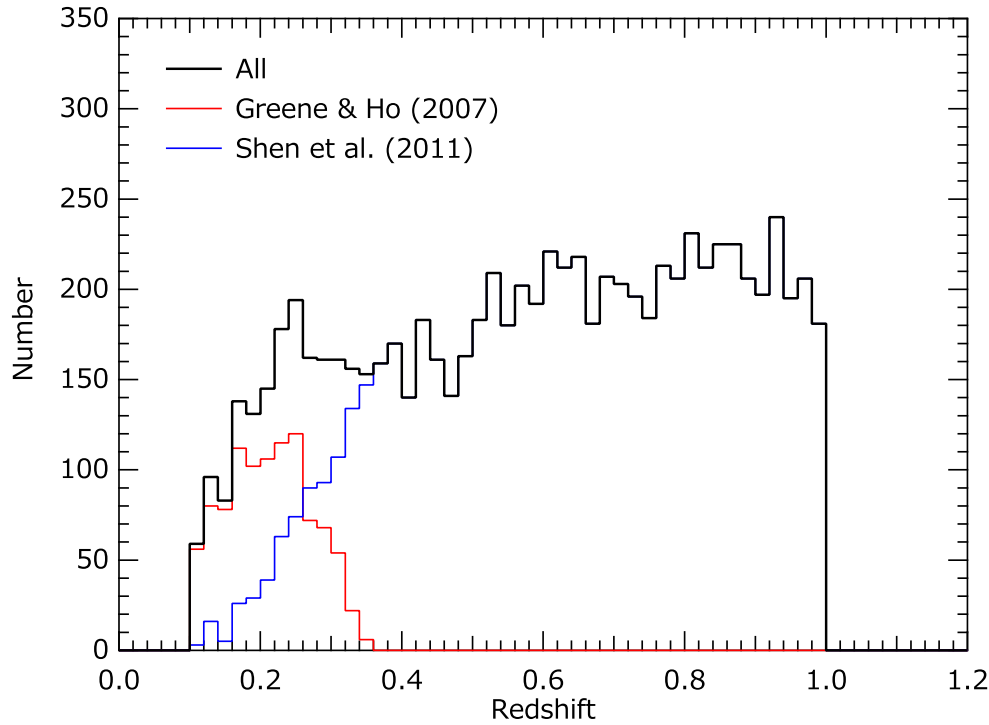


Fig. 4. Distribution of redshift for the same sample as shown in Figure 2. The red histogram with smaller redshift is for Greene et al. (2007a), the blue one is for Shen et al. (2011). The sum of them is shown with the black histogram.

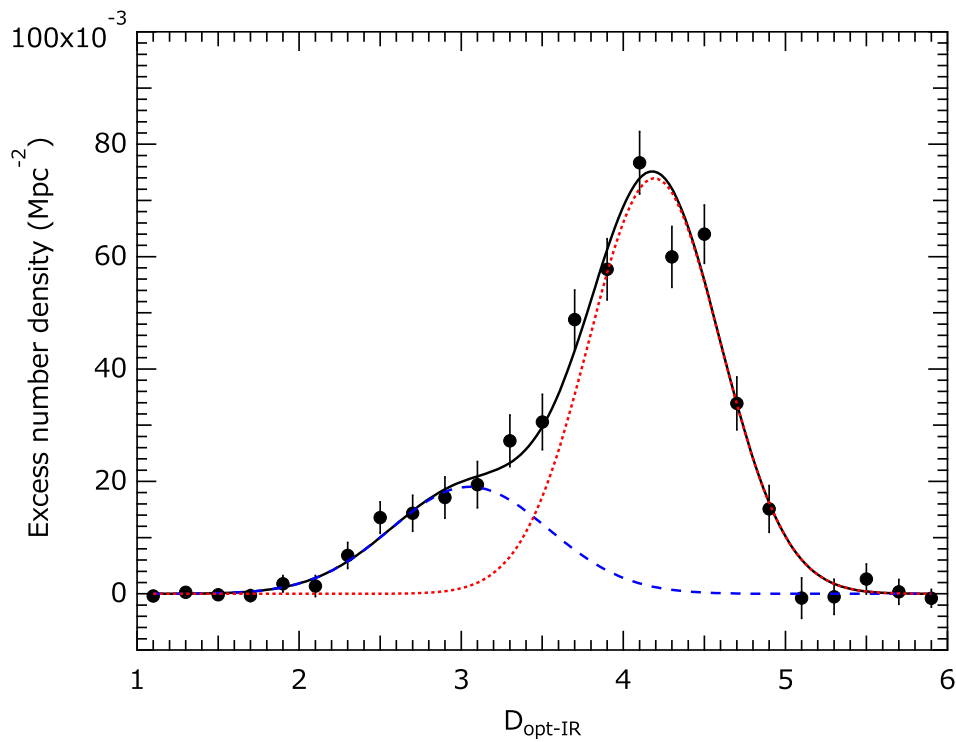


Fig. 5. $D_{\text{opt-IR}}$ parameter distribution for all the AGN samples is shown with filled black circles with statistical error bars. The distribution is fitted with a two Gaussian model (black solid line). Each component represented with a single Gaussian corresponds to blue cloud (peak with smaller $D_{\text{opt-IR}}$) and red sequence galaxies (peak with larger $D_{\text{opt-IR}}$).

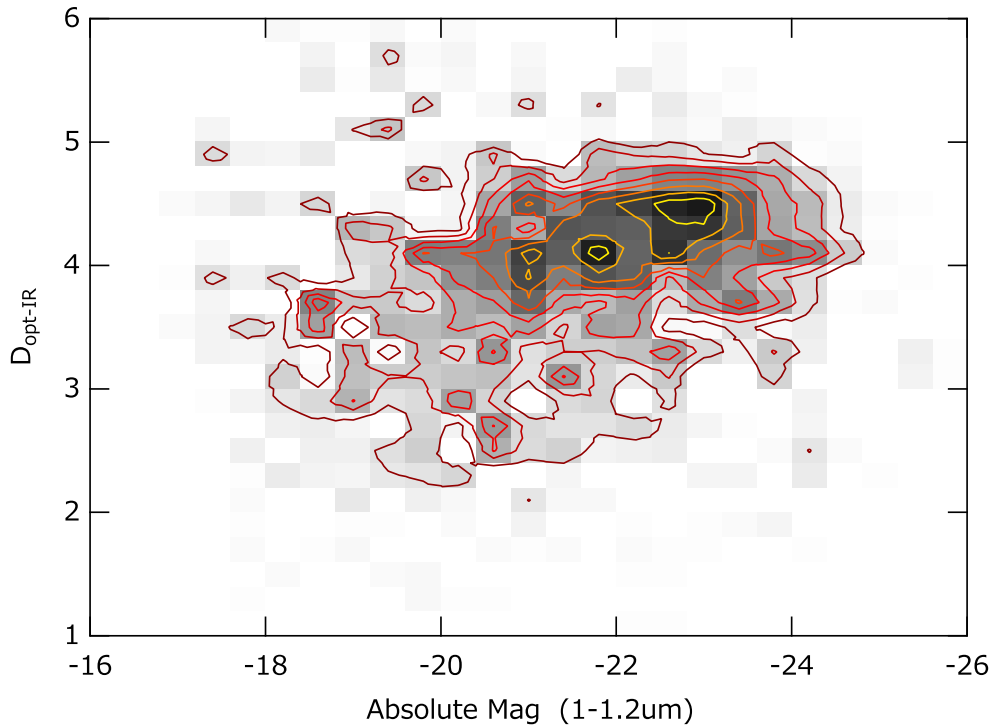


Fig. 6. Color magnitude distribution for all the AGN samples. Densities are represented with gray scales and contours of equi-density. Red sequence galaxies are concentrated in a upper right region ($M < -20$ mag and $D_{\text{opt-IR}} > 3.5$), while blue cloud galaxies are widely spread in the dimmer part.

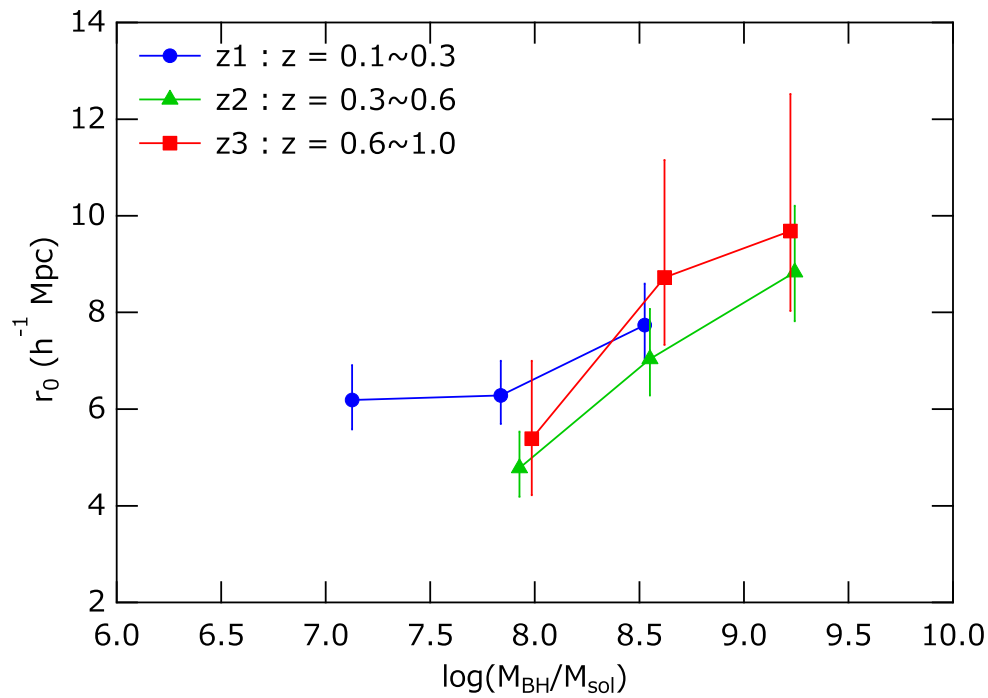


Fig. 7. Cross-correlation lengths derived for each redshift and mass group are plotted as a function BH mass. The data point of the same redshift groups are connected with a line. Solid circles are for z_1 redshift group, solid triangles and boxes are for z_2 and z_3 redshift groups, respectively.

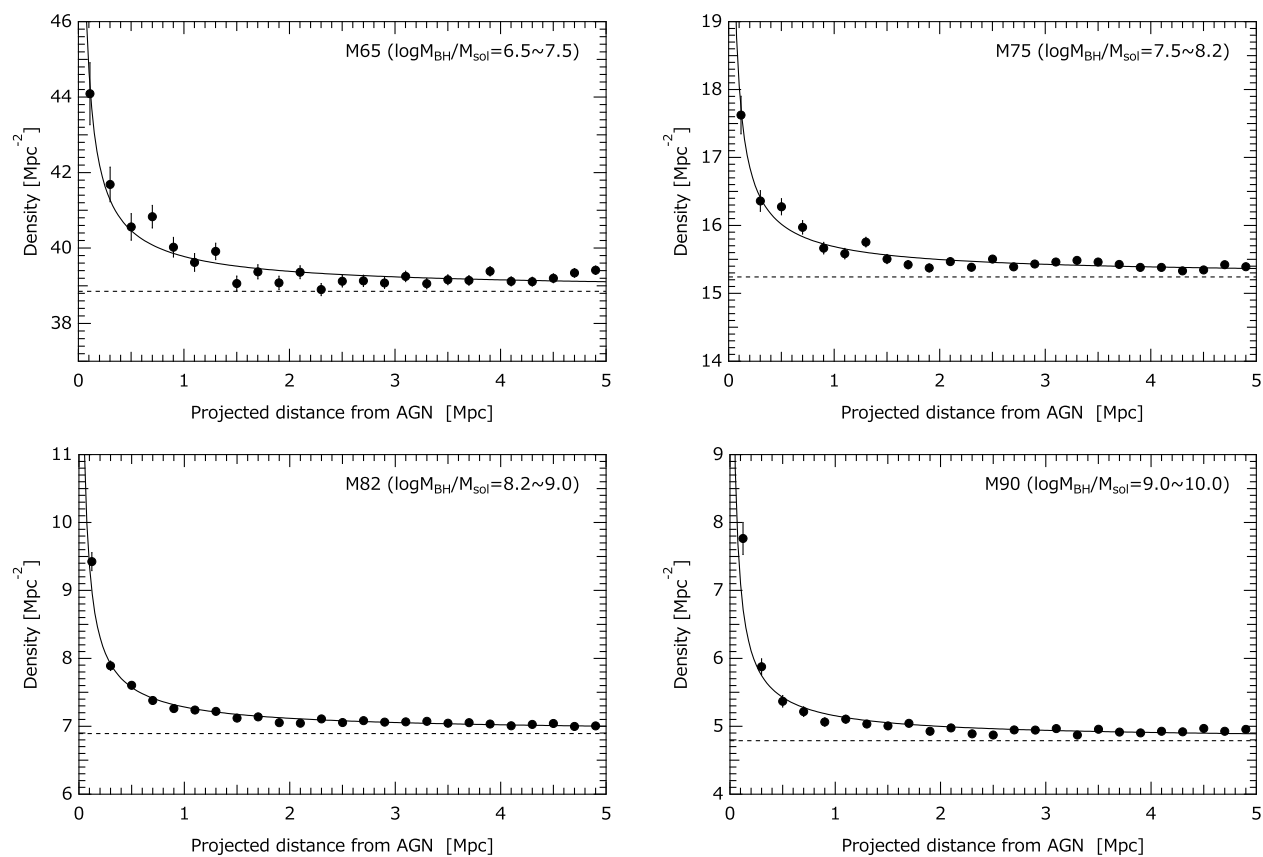


Fig. 8. Surface densities of galaxies plotted as a function of projected distance from AGN for mass group M65, M75, M82 and M90.

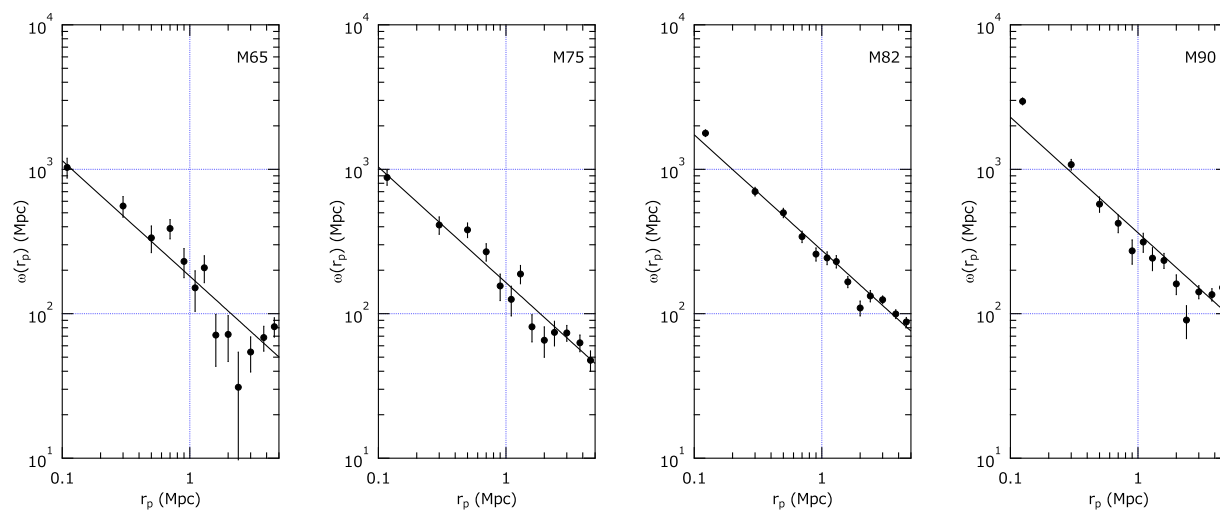


Fig. 9. Projected cross-correlation functions for mass group M65, M75, M82 and M90.

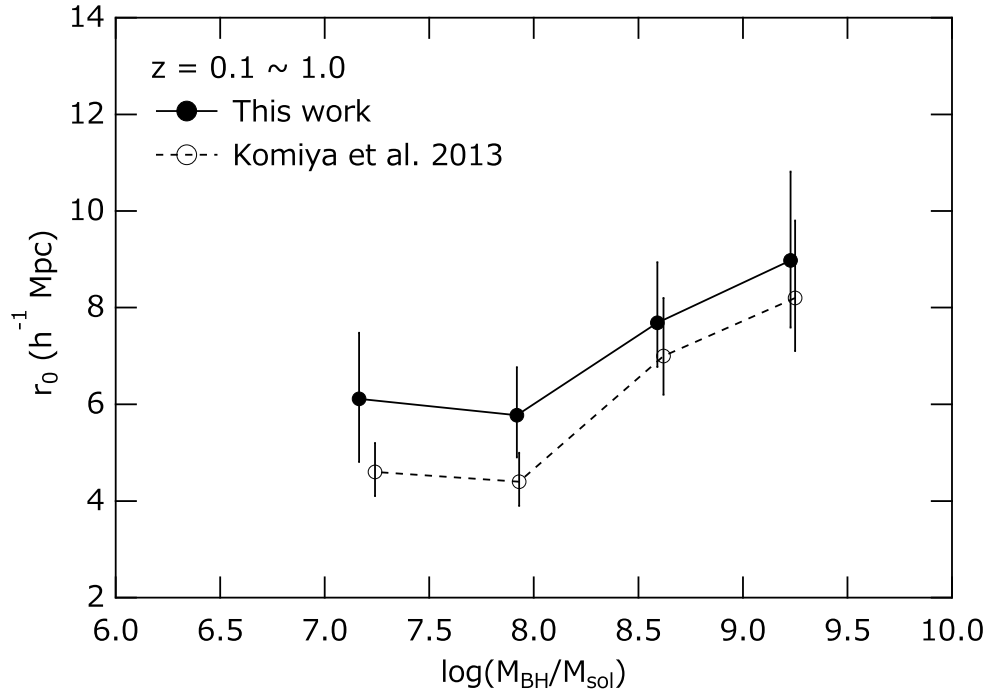


Fig. 10. Cross-correlation lengths derived for each mass groups are plotted as a function of BH mass. The redshift range of each mass groups are 0.1~0.3 for M65 mass group, 0.1~1.0 for M75 and M82 mass groups, and 0.3~1.0 for M90 mass group. Results of this work are shown with filled circles and previous work by Komiya et al. (2013) are shown with open circles. The error bars of this work include statistical error, systematic error, and uncertainty related with the intrinsic variance among AGNs.

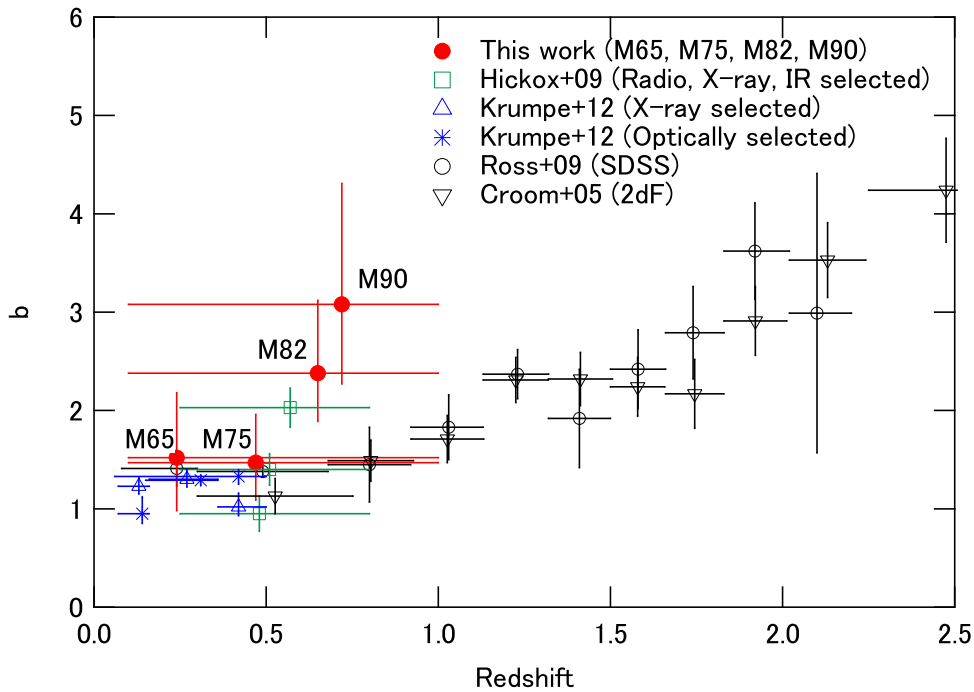


Fig. 11. AGN bias plotted as a function of redshift. The results of this work are plotted with filled circles for mass groups of M65, M75, M82 and M90. The results by Hickox et al. for radio, X-ray and IR selected AGNs are plotted with open squares at $b = 2.03$, 1.40, and 0.95, respectively. The results by Krumpe et al. for X-ray and optically selected AGNs, Ross et al. for SDSS QSOs, and Croom et al for 2dF QSOs are plotted with markers specified in the legend in this figure. The horizontal error bars represent the redshift range of the samples.

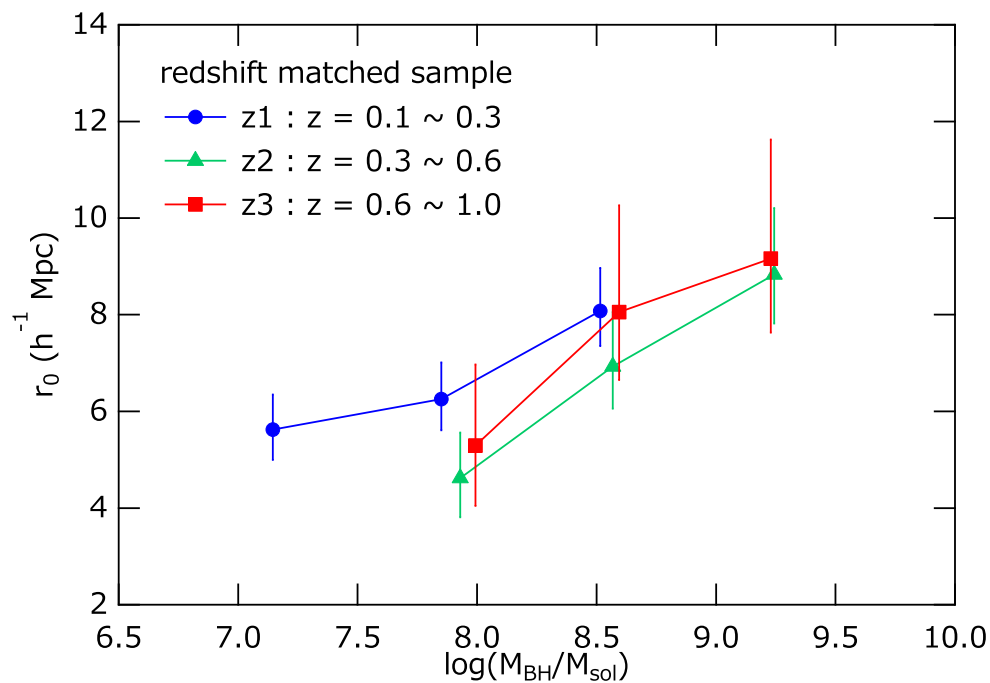


Fig. 12. Cross-correlation lengths derived for each redshift matched samples are plotted as a function BH mass. The data point of the same redshift groups are connected with a line. Filled circles are for z_1 redshift group, filled triangles and boxes are for z_2 and z_3 redshift groups, respectively.

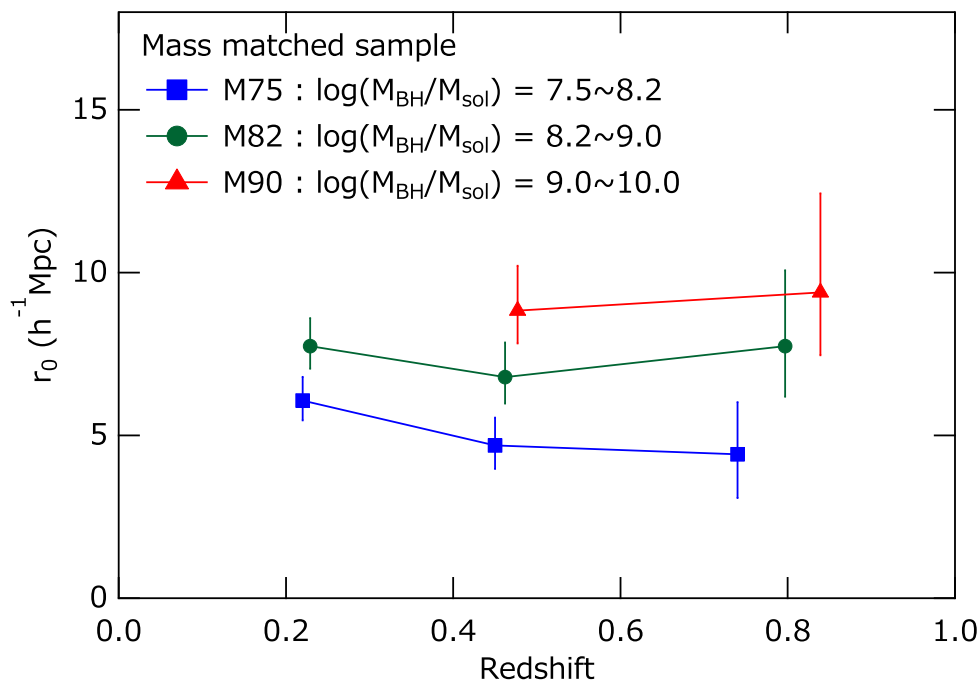


Fig. 13. Cross-correlation lengths derived for each BH mass matched samples are plotted as a function of redshift. The data point of the same mass groups are connected with a line. Filled boxes are for M75 mass group, filled circles and triangles are for M82 and M90 mass groups, respectively.

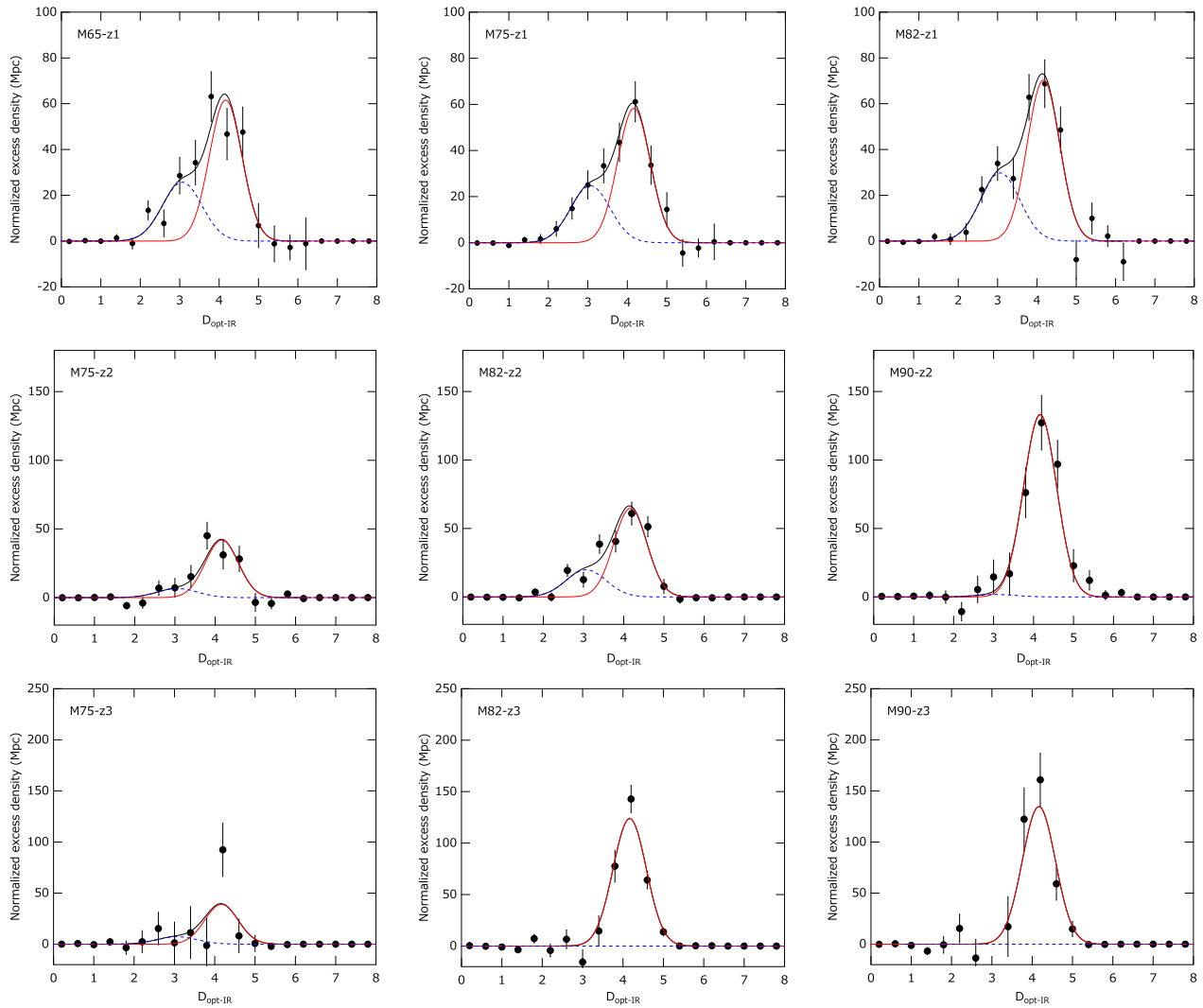


Fig. 14. Distributions of $D_{\text{opt-IR}}$ parameter for each redshift and mass groups. Filled circles represent observed data points, solid lines are fitting result of the two component model, red solid and blue dashed lines are for red and blue galaxy component, respectively.

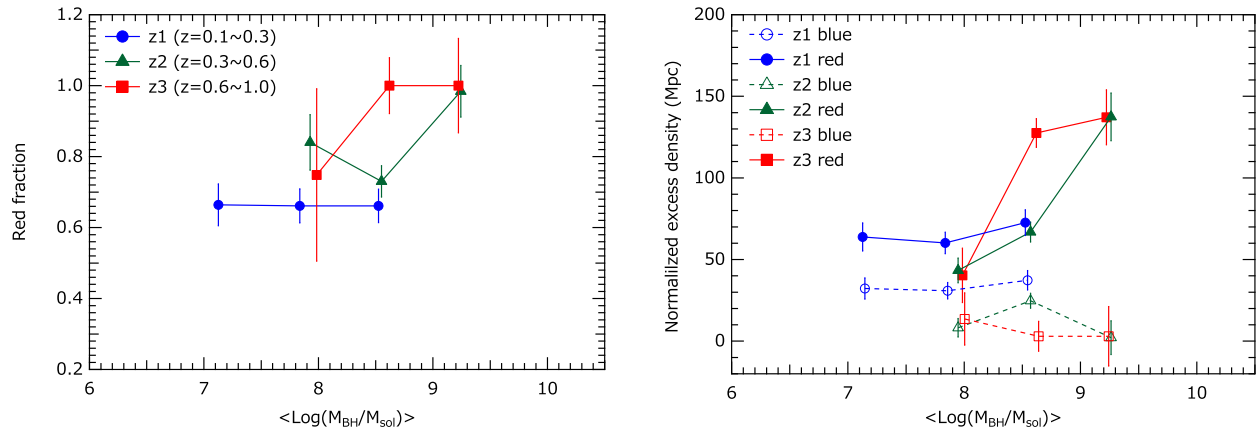


Fig. 15. Left panel: Red galaxy fractions derived from the two component fitting shown in Figure 14 are plotted as a function of BH mass. The results of the same redshift groups are connected with a line. Circles are results for redshift z1 group, and triangles and boxes are for redshift z2 and z3 groups, respectively. Right panel: Normalized excess density derived from the two component fitting. Filled and open circles are results for blue and red galaxies respectively for z1 redshift group. Filled and open triangles are results for z2 redshift groups with the same blue/red galaxy assignment. Filled and open boxes are results for z3 redshift groups with the same assignment, and the arrows represents the upper limit for blue galaxies at redshift z3.

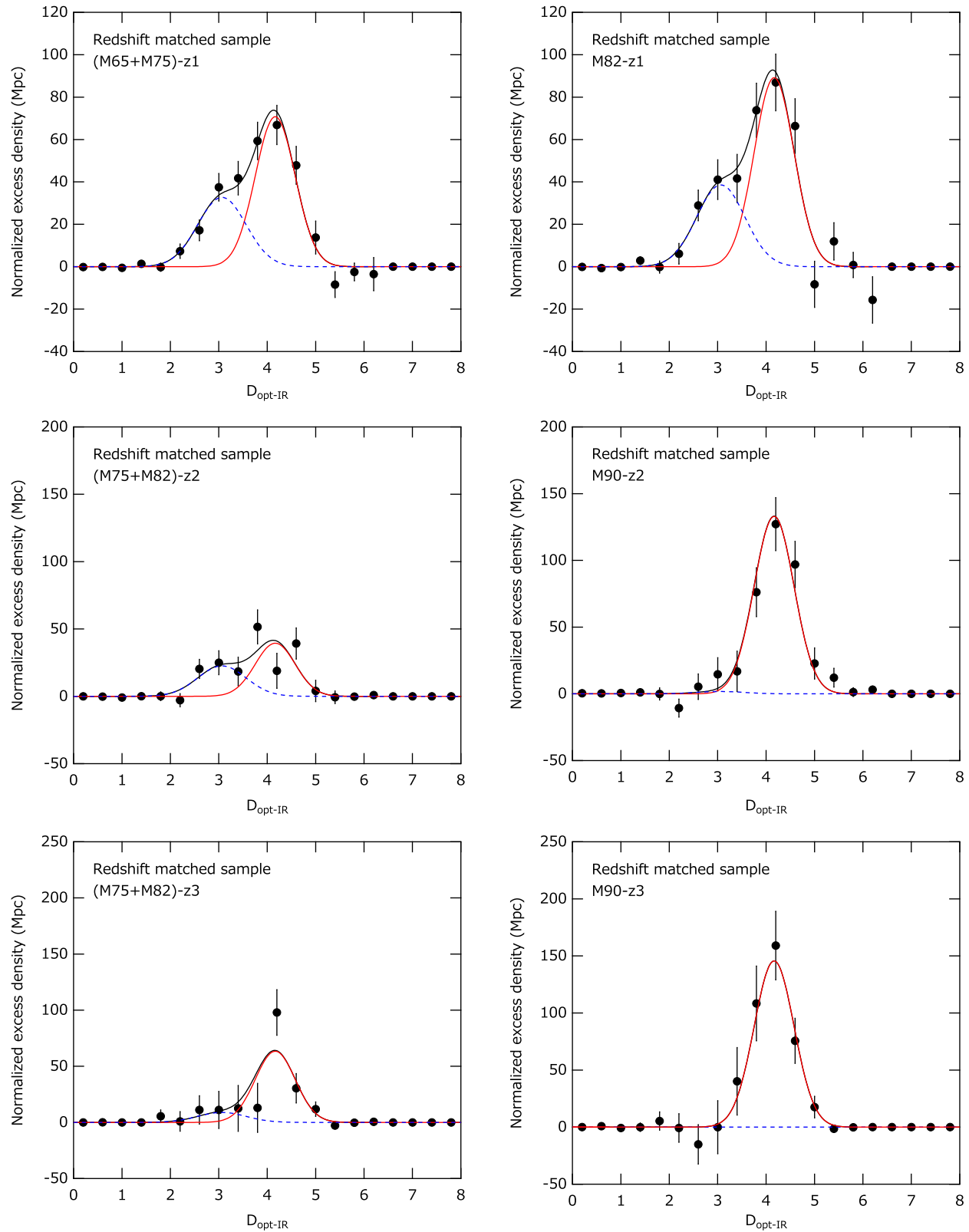


Fig. 16. Distributions of $D_{\text{opt-IR}}$ parameter for redshift matched samples. Filled circles represent observed data points, solid lines are fitting result of the two component model, red solid and blue dashed lines are for red and blue galaxy component, respectively.

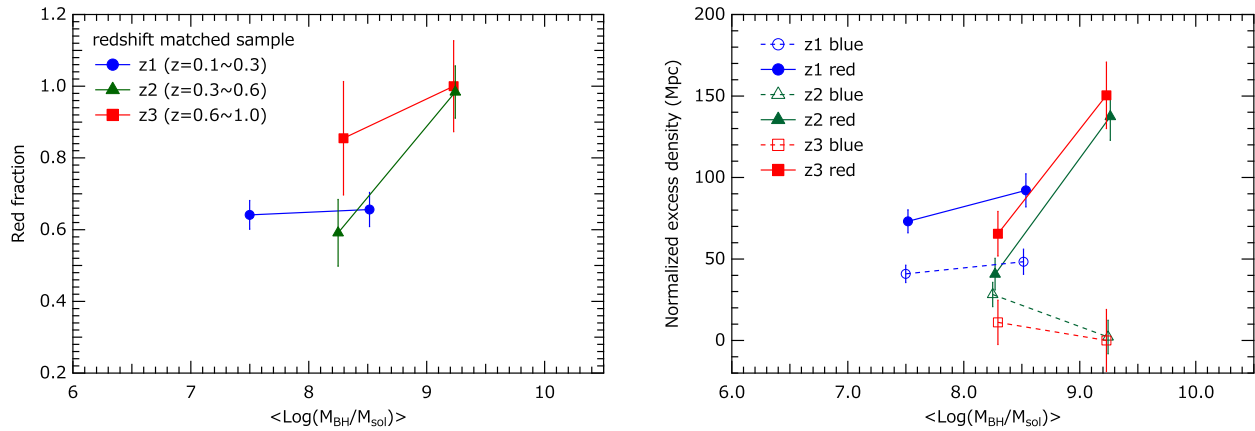


Fig. 17. Left panel: Red galaxy fractions derived from the two component fitting shown in Figure 16 are plotted as a function of BH mass. The results of the same redshift groups are connected with a line. Circles are results for redshift z1 group, and triangles and boxes are for redshift z2 and z3 groups, respectively. Right panel: Normalized excess density derived from the two component fitting. Filled and open circles are results for blue and red galaxies respectively for z1 redshift group. Filled and open triangles are results for z2 redshift groups with the same blue/red galaxy assignment. Filled and open boxes are results for z3 redshift groups with the same assignment.

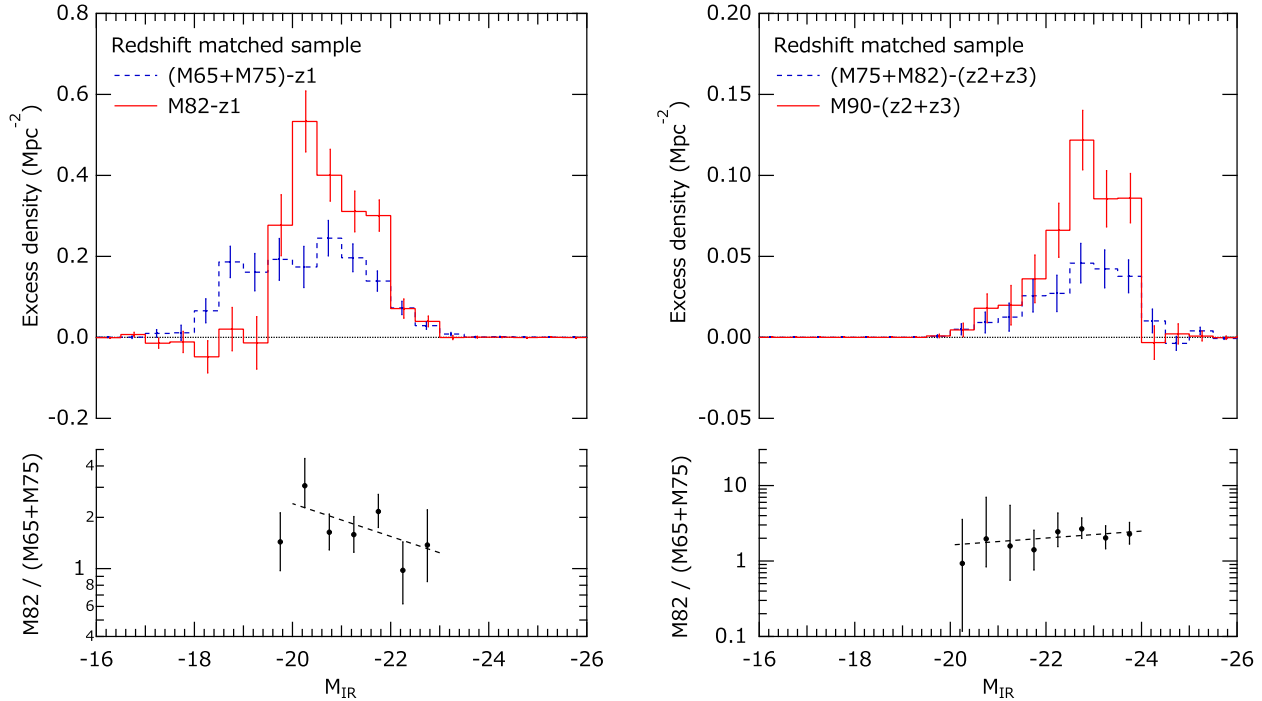


Fig. 18. Comparison of absolute magnitude distributions between higher (red histogram) and lower (blue histogram) mass groups. The ratios of high/low are plotted in the panel below the histograms. Dashed lines shown in the ratio plot is a result of a linear fit in linear-log scale.

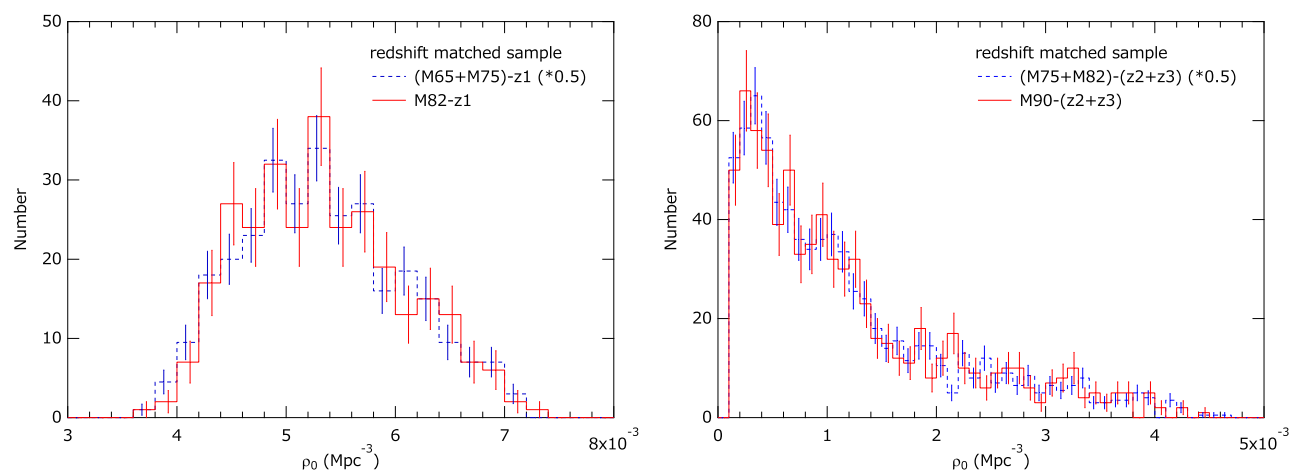


Fig. 19. Comparisons of the distributions of average number densities of galaxies at AGN redshift between higher (red histogram) and lower (blue histogram) mass groups. The left (right) panel is the comparison at redshift z_1 (z_2+z_3).

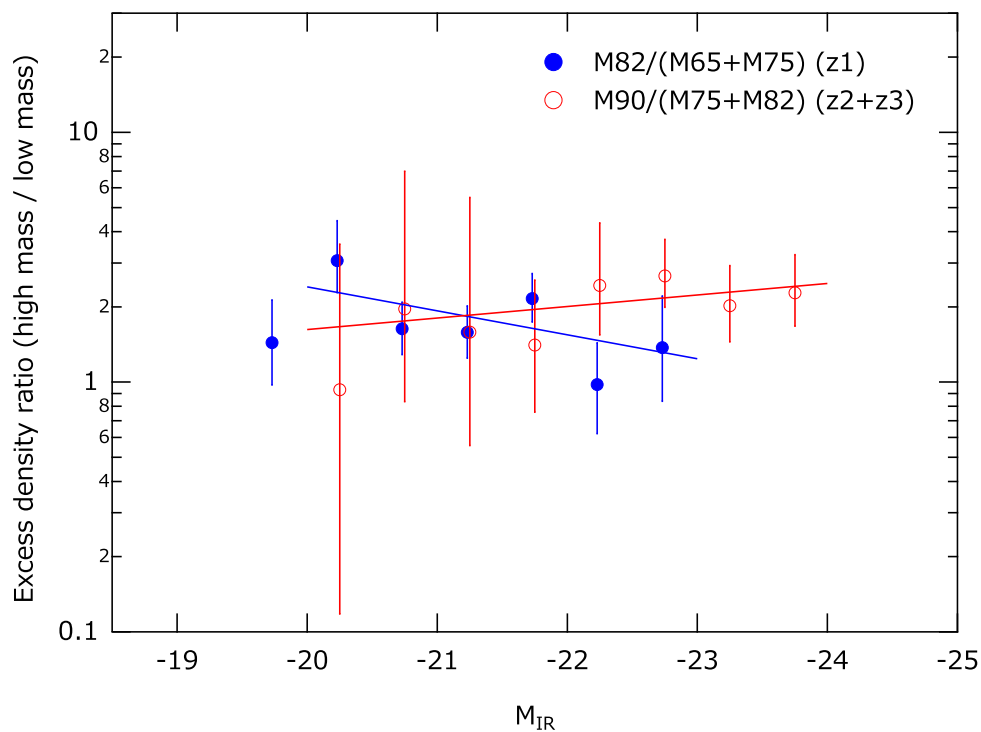


Fig. 20. Comparison of the ratio of absolute magnitude distributions. Filled blue circles represents the ratio of M82 and M65+M75 at redshift z_1 . Open red circles represents the ratio of M90 and M75+M82 at redshift z_2 and z_3 . Fitting results with a power law function are also shown with the solid lines.